

Extending the limit of widespread dispersed Toba volcanic glass shards and identification of new in-situ volcanic events in the Central Indian Ocean Basin

Ankeeta Amonkar^{*1, 4}, Sridhar D Iyer², E V S S K Babu³ and S Manju³

¹CSIR-National Institute of Oceanography, Dona Paula, Goa 403004, India.

²Formerly with CSIR-National Institute of Oceanography, Dona Paula, Goa 403004, India.

³CSIR-National Geophysical Research Institute, Hyderabad, Telangana, 500007, India.

⁴Marine Science, School of Earth, Ocean and Atmospheric Sciences, Goa University, Goa 403206, India.

(* corresponding author aamonkar@nio.org; ankeetaamonkar9@gmail.com)

Abstract

We report the widespread extent of Toba volcanic glass shards in the Central Indian Ocean Basin. Investigation of four sediment cores (7°S to 17°S) revealed several shard-rich horizons (SRH) that provide the first detailed tephrochronology for volcanic glass shards in the CIOB. A comparative study of surface sediments floored with Youngest Toba Tuff (YTT), indicate that irrespective of the rate of sedimentation, YTT in the basin is restricted to a depth of <35 cm-bsf. We utilized microtektites (0.77 Ma), associated with the Oldest Toba Tuff (OTT) glass shards, as a proxy for age calculation of the SRH. The results are comparable with well-established ages derived from paleomagnetic and $\delta^{18}\text{O}$ methods for the Leg 21 ODP Site 758.

The other significant finding of this study includes the first report of Middle Toba Tuff (equivalent to Layer C) and layer D that are present between YTT and OTT (Layer E) and also Layers G, H, h, I, J, K, L and M. All these layers correspond with those reported for ODP Site 758. Furthermore, two SRH between layers G and H show signatures of localized in-situ phreatomagmatic origin, suggesting that CIOB is apparently more active – tectonically and volcanically than it is presumed.

Keywords: Glass shards, Indian Ocean, Microtektites, Tephrochronology, In-situ events, Toba eruptive.

1.0 Introduction

Tephra layers in the marine sedimentary deposits have been extensively used to understand the cyclicity of volcanism, volcanic production rates, geochemical character of the source and temporal relations between paleoclimate and volcanism (Chesner et al 1991; Pattan et al 2002; Lowe 2011). Tephra layers act as stratigraphic event markers to help derive the tephrochronological history (Lane et al 2017) and can be effectively used to understand the global sedimentary system (Scudder et al 2009, 2016). Albeit with the advances in the identification of successive marine tephra layers, it is also equally important to date and correlate them with their proximal source and determine the aerial extent. Such correlation is mainly achieved through direct dating of sediments, however, in the marine environment it gets highly complicated as the tephra layers may not be well-defined and often blends with the sediments (Lane et al 2012), and in such a case indirect methods are used. The age of the sediments in the Central Indian Ocean Basin (CIOB) has been derived through biostratigraphy (Gupta 1988, 1996, 2009), radiogenic U-Th isotope dating (Banakar et al 1991; Nath et al 2013) and from the associated 0.77 Ma microtektites (Glass and Koeberl, 2006; Prasad et al 2007, Pattan et al 2010).

The volcanic glass shards that occur in the Indian Ocean sediments have been reported to be derived from the Toba volcano located in the Indonesian Volcanic Arc (IVA). The Toba volcano has erupted several times in the geological past and has led to the formation of the Haranggoal Dacitic Tuff (HDT, fission-track age 1.2 Ma; Nishimura et al 1977), Oldest Toba Tuff (OTT, $^{40}\text{Ar}/^{39}\text{Ar}$ age 0.80 Ma; Chesner et al 1991), Middle Toba Tuff (MTT, $^{40}\text{Ar}/^{39}\text{Ar}$ age 0.50 Ma; Mark et al 2017) and Youngest Toba Tuff (YTT, $^{40}\text{Ar}/^{39}\text{Ar}$ age 0.074 Ma i.e. 74 ka; Chesner et al 1991) while Storey et al. (2012) reported an age of 73.88 ± 0.32 ka for the YTT.

The HDT is recorded as the first large-scale eruption with a total surge of 35 km^3 (Chesner and Rose, 1991). This was followed by the OTT which erupted from the southern part of the Toba caldera and expelled tephra and dense rock equivalent that spread over $1,000 \text{ km}^3$ to $2,300 \text{ km}^3$ (Lee et al 2004; Pearce et al 2014). These tephra were welded and deposited on marine sediments of Palaeozoic and Mesozoic ages (Knight et al 1986). The glass shards of the OTT eruption are well-preserved in the CIOB sediments (Glass and Koeberl 2006; Pattan et al 2010; Iyer et al 2012; Pearce et al 2014). The MTT with an erupted volume of 60 km^3 (Chesner et al 1991) has a limited aerial extent and has been identified in ODP Leg 121 Site 758 core (henceforth we would be referring to this as Site

758, location 5°23.05'N, 90°21.67'E on the crest of Ninetyeast Ridge and about 1,000 km from the Toba volcano on Sumatra Island, Indonesia). Sanidine phenocrysts that were dated using the $^{40}\text{Ar}/^{39}\text{Ar}$ method showed an age of 0.501 ± 0.005 Ma (Diehl et al 1987; Chesner and Rose 1991; Mark et al 2017). Imbrie et al (1984) reported $\delta^{18}\text{O}$ stages for MTT to be between 13.2 and 14.2 which corresponds to ages of 0.513 and 0.538 Ma, respectively. Later, Dehn et al (1991) suggested the MTT to be Layer C in Site 758.

Of all the four eruptions, the YTT was a super-eruption that resulted in a large-scale dispersion of the ash (rhyolitic glass shards) that covered an area of at least 4×10^6 km² (Rose and Chesner 1987). Using age dispersal model, Costa et al (2014) estimated that the YTT fallout of 8,600 km³ covered an area of 40 million km² and the volume of eruptive materials to be 5,800 km³. The significant presence of the YTT in the north-eastern Indian Ocean was reported earlier (Ninkovich et al 1979; Kennett 1981; Dehn et al 1991). Later works have revealed that the YTT has been dispersed as far as to Antarctica (Song et al 2000), the Indian subcontinent (Acharyya and Basu 1993; Shane et al 1995; Westgate et al 1998; Srivastava and Singh 2019), CIOB (Iyer et al 1997; Pattan et al 1999, 2010; Pearce et al 2014), Bay of Bengal (Gasparotto et al 2000), Malaysia (Gatti et al 2012) and South China Sea (Wiesner et al 1995; Song et al 2000; Bühring et al 2000; Liu et al 2007).

The YTT eruption occurred near the marine isotope stage 5-4 boundary (Schulz et al 2002) and led to global cooling (Oppenheimer 2002; Williams et al 2009). Rampino and Self (1993) suggested that the super-eruption of Toba resulted in volcanic winter and accelerated glaciations. But according to Schulz et al (2002), this may not have been the case, on the contrary, they suggested that the Toba eruption may have had a minor impact on the evolution of the low-latitude monsoonal climate. The Toba eruption perhaps affected the tropical ecosystem, increased deforestation and caused a near extinction of humans (Rampino and Self 1993; Gathorne-Hardy and Harcourt-Smith 2003; Williams et al 2009).

The distribution of tephra in the Indian Ocean is also supported by enhanced ϵ_{Nd} values at ODP Site 758, 757 and 707 in the Indian Ocean. Gourlan et al (2008) opined that a cyclic increase in the ϵ_{Nd} values could be a result of addition of radiogenic Nd from the Indonesian volcanic environment. Banerjee et al (2019) have reported the radiogenic concentration of Sr and Nd from ODP Site 758A and suggested changes in the palaeoceanographic condition during mid-Miocene. These changes in the radiogenic isotope concentration could be a result of the different eruptions that occurred from 14 Ma to Recent near the ODP Site 758.

With growing interest to understand deep-sea volcanism, new insights from tephra studies could help answer several issues among which one of the most important is to understand the type and source of tephra (either transported from aerial eruptions or derived from deep-sea eruptions) that occurs at a water depth of 5,000 m and more in the CIOB. Previous studies of the CIOB reported volcanic glass shards to be ubiquitously present in the surface sediments and in short (<35 cm) and long sediment cores (~5 m). The glass shards were observed to be dispersed in the top few centimetres of the sediment while in most of the short as well as long cores the abundance was confined to layers/horizons occurring at variable depths (Banakar et al 1991; Pattan et al 1999, 2002; Prasad et al 2007) (Table 1). We have referred to such layers as shard-rich horizons (SRH). Prior investigations of the CIOB, have detailed the glass shards in terms of their morphology, composition and possible origin (Iyer et al 1997; Mascarenhas-Pereira et al 2006, 2016).

Based on the existing reports the glass shards occurring in the CIOB are either of ex-situ or in-situ origin. The former source for the glass shards has been exclusively ascribed to the Toba volcano (Martin-Barajas and Lallier-Verges 1993; Pattan et al 2010; Glass and Koeberl 2006). These shards are of the OTT and YTT and are amongst the well-known Toba eruptions in the basin (Glass and Koeberl 2006; Pattan et al 2010; Iyer et al 2012; Pearce et al 2014). In contrast, there are limited reports of the in-situ or intra-basinal formation of glass shards in the CIOB (Iyer et al 1997; Sukumaran et al 1999; Mascarenhas-Pereira et al 2006). Mascarenhas-Pereira et al (2016) have reported in-situ strombolian-type glass shards that correspond to 85, 107-109, and 142-146 ka and a crypto-tephra layer of 34 ka (Table 1).

Based on the above cited studies it is evident that there has been little attempt to determine the possible source of SRH in the basin, the sequential events of deposition of the various SRH and possibility of widespread in-situ strombolian events that occurred in space and time. Therefore, in the present study, we have classified the identified SRH to understand the ex-situ and in-situ variants and propose a systematic tephrochronology for the SRH present in the CIOB.

2.0 Study Area

The CIOB is the largest basin in the Indian Ocean and extends between latitudes 6°S to 20°S and longitudes 72°E to 80°E, and has an average water depth of 5,000 m (Mukhopadhyay et al 2018). The basin holds signatures of deformation, fracture zones (FZ), faults, lineations, abyssal hills, and hundreds of seamounts. The basin formed between 60 and

50 Ma as a result of the Indo-Eurasian tectonic plate collision followed by a progressive northward movement of India (Das et al 2005, 2007). The northern region of the CIOB is affected by voluminous sediment load from Ganges and Brahmaputra rivers. In the central region siliceous sediments are dominant while red-clay is present towards the south below 15°S (Udinstev 1975; Kolla and Kidd 1982). The occurrence of carbonate preservation in calcareous sediment over a seamount summit has also been reported (Nath et al 2013). Deposits of ferromanganese (FeMn) nodules and crusts are abundant in the siliceous sediments and these have been well studied together with the associated volcanic, sediments and hydrothermal materials (Iyer 2007).

3.0 Materials and Methods

The four gravity sediment cores considered in this study (Figure 1) were collected in the year 1999 onboard research vessel *A.A. Sidorenko* (cruise AAS-22) during deep-towed operations under the polymetallic nodule expedition (Table 1). The northern cores AAS-22/8 and AAS-22/7 were collected from the siliceous sediment while the cores AAS-22/5 and AAS-22/3 were recovered from the transition of siliceous pelagic and pelagic sediments respectively.

All the four cores were sub-sampled at 5 cm interval and oven dried at 60-70 °C to remove the water content. About 25 g of each of the dried sub-samples was treated with 20 ml of 10% Na-hexametaphosphate and kept overnight to disperse the clay minerals. Subsequently the samples were wet sieved using a 63 µm mesh sieve. The coarse fractions (CF >63 µm) recovered after sieving were oven dried and prepared for further examination. The percentage of CF was calculated based on the recovered fraction subtracted by the loss of dry sediment.

The CF were observed under an Olympus SZX7 binocular microscope at magnifications ranging between ×8 and ×56. Furthermore, 0.10 mg of the dried sediment samples were obtained using a coning quartering method and from these the glass shards were visually counted under the binocular microscope. The data are presented in Table 2.

Several components, including glass shards from each SRH, were handpicked, affixed on carbon adhesive pasted over plastic mounts and carbon coated. The mounted grains were examined under a Scanning Electron Microscope (SEM) for their morphological and surface features using Leica Model 440 with a working distance of 20 mm and accelerating voltage

of 20 kV and a dead time of 20% at CSIR-National Institute of Oceanography, Goa and National Centre for Polar and Ocean Research, Goa.

Major element compositions of glass shards were determined using a Cameca SX 100 Electron Probe Micro Analyser (EPMA) at the CSIR-National Geophysical Research Institute, Hyderabad, India. The operating conditions were 20kV accelerating voltage, 5 μm beam diameter and 20 nA beam current. All the elements were analysed sequentially using wavelength dispersive spectrometry (WDS). To overcome alkali-loss issues while analysing glasses, Si, Na, and K were analysed simultaneously on three different spectrometers. To improve the quality of some low abundance elements (Ti and Mn), an analytical strategy of integrating data from the analysis on more than one spectrometer was used. This resulted in <0.5% error for the major elements. Tektite standard USNM 2213 analysed by USGS (Jarosewich et al 1980) was used during the analysis and accuracy of the data was better than $\pm 0.4\%$. Mid-oceanic ridge basalt glasses were used to monitor the quality of the analysis. ZAF corrections were incorporated before finalizing the data. The compositional data were recalculated to 100 with the difference being H_2O .

4.0 Results

4.1 Core descriptions

The four sediment cores were examined for their physical appearance and components present in the CF. In general, binocular microscopy of the $>63 \mu\text{m}$ CF revealed an assemblage of mainly radiolarians, FeMn micronodules ($<1 \text{ cm}$ size), basaltic fragments, palagonite grains, volcanic glass shards, microtektites, pumice pieces, bread crust (oxidised basaltic glass), magnetite spherules, biotite flakes and phillipsite crystals (Amonkar and Iyer, 2017). The plot of the CF against core depth (Figure 2) portrays variations in the major components such as radiolarians, glass shards, FeMn micronodules, and palagonite grains. Radiolarians are overwhelming in the northern cores (AAS-22/7 and AAS-22/8) but are substantially less in the southern ones (AAS-22/3 and AAS-22/5). We present the detailed description of each core (starting from the northernmost core) in terms of their CF, and layer-wise abundance, morphology and chemistry of the glass shards occurring in the SRH (Figure 2).

4.1a Core AAS-22/8: This core is located towards the northern extreme (7°S) in the siliceous sediment domain (Table 1; Figure 1) and throughout its length has a moderate yellowish brown (10YR 5/4). Lenses of dark yellowish brown (10YR 4/2) occur at a core depth of 38-

40, 485-490 and 520-525 cm-bsf (below seafloor). FeMn nodules (smooth, nearly rounded and up to 2 cm diameter) are present at a depth of 245-250 cm-bsf.

The down-core plot (Figure 2) depicts a linear trend in the CF up to 100 cm-bsf with CF ranging from 2 to 3% while below 100 cm-bsf the CF is slightly higher (4 to 5%). The low CF% in the upper 100 cm-bsf of the core is due to the occurrence of only radiolarians. Distinct large peaks were observed at core depths of 210, 230, 435 and 530 cm-bsf, and relatively smaller peaks at 140, 190, 350 and 370 cm-bsf. Most of these peaks are mainly due to abundant glass shards while those at depths 230, 350 and 370 cm-bsf are due to FeMn micronodules (Figure 2). Abundant microtektites that are present between 205 and 210 cm were attributed to the Australasian tektite strewn field (0.77 Ma age) (Prasad et al 2007).

In core AAS-22/8 we identified six SRH occurring at depths of 135-140, 190-195, 205-210, 430-435, 485-490 and 520-520 cm-bsf (Table 2; Figure 3). The glass shards in the upper SRH are colourless and show cusped and Y-shaped intersections (Figure 4) while those at depths 485-490 and 520-525 cm-bsf are blocky and have a smooth surface (Figure 5). The glass shard counts per 0.1 mg of the sediment are 2,133 (135-140 cm-bsf), 3,482 (190-195), 4,607 (205-210), 2,972 (430-435), 2,586 (485-490), and 3,507 (520-525 cm) (Table 2).

The chemical data of the glass shards show high silica (73-74 wt.%) and high abundance of total alkalis (5 wt.%) with very low concentrations of MgO (0.04-0.06 wt.%), MnO (0.06 wt.%) and TiO₂ (0.05 wt.%) and moderate contents of CaO (0.7 wt. %) and FeO (0.9 wt.%) (Table 3). The Na₂O/ K₂O ratio is very low (0.2-0.3) in the shards with cusped morphology but is slightly higher (≥ 3.3) for the blocky shards.

4.1b Core AAS-22/7: This core located at 10°S (Table 1; Figure 1), is about 330 km south of core AAS-22/8 and has a similar textural appearance. This core does not show much variation in terms of physical properties as it is also located in the siliceous domain.

Throughout the core length, the CF is dominated by radiolarians and the drastic down-core change in the CF% is mainly due to the plentiful occurrence of FeMn micronodules and basaltic material. Two distinct SRH were observed at depths of 0-5 and 220-225 cm-bsf (Table 2; Figure 3). The latter SRH has abundant microtektites of light green to pale yellow colour, rounded to sub-rounded in shape and are easily distinguished by their pitted/cratered surface. These microtektites again correspond to the Australasian tektite strewn field (Prasad et al 2007). The glass shards have a cusped, bubble wall morphology. The highest number of

shards was observed at depth 0-5 cm-bsf (4,593) while those associated with microtektites showed 4,170 counts (Table 2).

The chemical analysis of the shards shows SiO₂ to be slightly higher (72-78 wt.%) compared to the adjacent core AAS-22/7, while total alkalis are 5.4-5.6 wt.%. Similar to AAS-22/7, the SRH also show very low concentrations of MgO (0.04-0.05 wt.%), MnO (0.06 wt.%), TiO₂ (0.05 wt.%), CaO (0.75 wt.%), and FeO (0.9 wt.%) (Table 3) and Na₂O/ K₂O ratio (~0.3).

4.1c Core AAS-22/5: This core retrieved from the transition zone of siliceous and red clay sediments (Table 1; Figure 1) has a moderate brown colour (5YR 4/4). Highest CF (~10%) is observed in the top section of the core with FeMn micronodules at a depth of 20-30 cm-bsf. The fluctuations in the CF% were observed up to a depth of 140 cm-bsf, and below this depth the CF% either gradually increases or decreases with increasing core depth (Figure 2). The broad peak at depth 290-370 cm-bsf was noted to be due to palagonite grains and FeMn micronodules. Three SRH occur in this core at depths 10-15, 110-115, and 245-250 cm-bsf (Table 2; Figure 3); out of these the SRH at depth 110-115 cm-bsf is associated with abundant microtektites (cf. Prasad et al 2007). The glass shards show cusped and bubble wall morphology in all the three SRH. The shard count analysis is 3,044 (10-15 cm-bsf), 2,915 (110-115 cm-bsf) and 1,690 (245-250 cm-bsf) (Table 2).

The chemical data for the three SRH layer show consistent SiO₂ (73 wt.%) along with MnO (0.05-0.07 wt.%), MgO (0.04-0.05 wt.%), CaO (0.7 wt.%), and FeO (0.9 wt.%). The SRH at depth 245-250 cm-bsf show slightly higher values for FeO (1.09 wt.%), TiO₂ (0.13 wt.%), MnO (0.08 wt.%), MgO (0.14 wt.%), and CaO (1.01 wt.%) and low values for Al₂O₃ (11.9 wt.%), K₂O (3.17 wt.%) and Na₂O+K₂O (4.2 wt.%) (Table 3). The Na₂O/ K₂O ratio is low 0.2-0.3.

4.1d Core AAS-22/3: This southernmost core is composed of deep brown colour (5YR 3/4) pelagic clay (Table 1; Figure 1). Overall, the CF % is very low (2-3%) compared to the other cores used in the present study and Fe micronodules occur at depths of 0-10 cm and 40-45 cm-bsf. The CF peak at 280-300 cm-bsf (Figure 2) is attributed to glass shards, while multiple peaks below 400 cm-bsf are mainly due to the presence of FeMn micronodules. In this core, we observed nine SRH at depths of 10-15, 60-65, 170-175, 285-290, 295-300, 325-330, 335-340, 350-355 and 365-370 cm-bsf (Table 2; Figure 3). The shards have similar morphology i.e. cusped, bubble wall and Y-shaped intersections (Figure 4). The shard counts

at various depths are 4,973 (10 -15 cm-bsf), 3,322 (60-65), 2,025 (170-175), 1,600 (285-290), 3,214 (295-300), 2,800 (325-330), 1,882 (335-340), 2,153 (350-355), and 2,100 (365-370) (Table 2).

The chemical analysis of the eight identified SRH layers shows SiO₂ from 72-75 wt.%, total alkali from 5.4-5.9 wt.%, MgO (0.04-0.06 wt.%), MnO (0.05-0.07 wt.%) and TiO₂ (0.05-0.06 wt.%) (Table 3). The Na₂O/ K₂O ratio is low 0.2-0.3.

The compositions of the glass shards of the four cores were plotted on the TAS diagram (Figure 6A). It was observed that the shards fall in the field of rhyolite. The plot of SiO₂ against CaO shows an inverse relation indicating decreasing CaO with increasing SiO₂ (Figure 6B).

5.0 Interpretations

Based on the observation of all the four sediment cores it is noted that there has not been any disturbance of the sediment after being deposited. This is based on the fact that (i) bioturbation and its effects were not visible as evident from the absence of mixing of the sediment layers and trails and burrows within the cores, and (ii) there are no signatures of alteration associated with the glass shards as observed from their fresh appearance (Figures 4 and 5). The location of the four sediment cores along a transect line has been used to trace the continuity and stratigraphy of the SRH within the CIOB. Mascarenhas-Pereira et al. (2006) ruled out the possibility of shards from adjoining sources and have suggested the shards to be either from Toba or in-situ. Hence in the present work, the identified layers have been compared with ODP Site 758 (Dehn et al 1991) to understand the widespread distribution of Toba glass shards in the CIOB.

Morphology and size are important parameters to understand the distribution, formation, and origin of the shards. In general, the shards range in size from 30 to 720 µm. Based on the morphological observations, we have classified the shards into two types: (I) cusped with Y-shaped intersections and contains vesicles (Figure 4) and (II) smooth surfaced and blocky shards that are either non-vesicular or poorly vesiculated (Figure 5). We noted that most of the SRH had type I glass shards except two SRH in the core AAS-22/8 (Figure 5) at depth of 485-490 and 520-525 cm-bsf that has type II glass shards. We observed a significantly higher number of glass shards in the top section of all the three cores (Table 2) at depth 0-5 cm in AAS-22/7 (4,593 number), 10-15 cm in AAS- 22/5 (3,044) and at 10-15 cm in AAS-2/3 (4,973). While a similar abundance was observed in AAS-22/8 at depth 205-

210 cm (4,607), AAS-22/7, 220-225 cm (4,170), AAS-22/5, 110-115 cm (2,915), and AAS-22/3, 60-65 cm (3,322). This fact suggests some major volcanic inputs for the glass shards in the basin other than from Toba eruptive.

5.1. Sedimentation rate and age of the cores

Before correlating the SRH in our cores with the identified layers in ODP 758, it was important to derive the age of the sediments in which the SRH are present. The rate of sedimentation and chronological dates for the CIOB sediments have been determined using sequential biostratigraphy and radiolarians proxies (Gupta 1988, 1996, 2009) or U-Th isotopic compositions (Banakar et al 1991; Nath et al 2013 and references therein). Besides these methods, Australasian microtektites that occur within the sediment cores have also been used to obtain the sediment age and sedimentation rate. This is because the Australasian tektite strewn field is known to have a widespread distribution and covers an area of over more than 50 million km² including a large region of the Indian Ocean (Wittke et al 2013). The youngest Australasian tektite strewn field is one of the largest of the major four fallouts during the Cenozoic times and is well traceable in the CIOB (Prasad et al 2010 and references therein). Because this event is dated to be of 0.77 Ma age (Kunz et al 2000; Prasad et al 2013; Mark et al 2017), the presence of abundant microtektites at a particular core depth is a valuable chronological marker horizon to calculate the sedimentation rates (e.g. Glass and Koberl, 2006; Prasad et al 2007; Pattan et al 2010). A similar approach of using the Australasian microtektites was made by Lee et al. (2003) for three deep-sea cores located 1,800-2,500 km away from the Toba caldera and along an east-west transaction across the South China Sea. In view of the above reports, we have used the well-established ages of Australasian microtektites as a diagnostic indicator to calculate the rate of sedimentation.

We observed microtektites at a much shallower depth in the cores towards the south of the study area. For example, microtektites in cores AAS-22/8 are between 205 and 210 cm-bsf, AAS 22/7 (220-225 cm-bsf), and AAS-22/5 (110-115 cm-bsf) while in the southernmost core AAS-22/3 microtektites occur between 60 and 65 cm-bsf. These depths were compared with those for the same cores by Prasad et al. (2007). We noted that the reported depths match well with our observations, indicating that these depths represent the datum plane of 0.77 Ma age. The abundance of microtektites within the study area could be due to the changes in the sedimentation rate from north to south in the basin (Udintsev, 1975; Banakar et al 1991; Borole, 1993; Gupta et al 1988; Nath et al 1989, 2001).

Pattan et al (2010) opined that in the Indian Ocean the coexisting layers of OTT and microtektites have merged and hence could be used as a marker. Therefore, considering this co-occurrence of microtektites (age 0.77 Ma) and glass shards (OTT) in the core AAS-22/8, we calculated the sedimentation rate to be 2.69 mm/ka. While for the other three cores the sedimentation rate is based on the presence of glass shards from the sediment surface to the YTT layer and YTT to OTT layers. We obtained a sedimentation rate of 0.34 mm/ka up to YTT and 3.1 mm/ka from YTT to OTT for the core AAS-22/7 (Table 5). The high CF %, abundance of radiolarian and diatoms and higher sedimentation rate in the northernmost cores (siliceous sediment) indicate this area to be influenced by equatorial upwelling. The sedimentation rates for the southern core AAS-22/5 (siliceous-pelagic transition) is 1.68 mm/ka up to YTT and 1.43 mm/ka from YTT to OTT and for the core AAS-22/3 (pelagic clays) the rates are 1.68 mm/ka from the surface to a depth of 15 cm (YTT) and 0.718 mm/ka between YTT and OTT (Table 5). The calculated sedimentation rates are remarkably close to the reported values of 1.7 mm/ka (above YTT) and 0.718 mm/ka (YTT to OTT) (0.72 by Pattan et al 2010).

Apart from these calculated sedimentation rates in the CIOB, Goldberg and Koide (1963) recorded a sedimentation rate of 2.75 mm/ka using Ionium/Thorium methods for the Indian Ocean sediments. While, Banakar et al. (1991) and Borole (1993) determined a rate of 1-5 mm/ka using the ^{230}Th method. Based on radiolarian biostratigraphy, Gupta (1991) reported a sedimentation rate of 2.5 mm/ka for the CIOB sediments, while ^{230}Th decay studies indicated the rate of sedimentation to be 2.3 mm/ka along 10°S to 14°S latitudes and 75°E longitude (Mascarenhas-Pereira et al 2006). In summary, the sedimentation rates in the CIOB vary between 1 and 5 mm/ka and our results fall well within these rates (Table 2). Therefore, we will be using our above-derived rates throughout this paper.

5.2. Tephrochronology of the SRH from CIOB

Palaeomagnetic (Diehl et al 1987) and $\delta^{18}\text{O}$ dates for Site 758 (Dehn et al 1991) have been used to correlate with the present study to derive a sequential tephrochronology for the SRH in the CIOB. Based on the global distribution of the YTT (Lane et al 2017), its occurrences in the CIOB (Pearce et al 2014), distinct morphology (cusate and Y shape intersections) and rhyolitic chemical composition, we infer that occurrence of SRH in the cores AAS-22/7 (0-5 cm-bsf) and AAS-22/5 (10-15 cm) is equivalent to the YTT. This is also attested by our synthesis of the previous studies (Table 1) which indicate that the YTT occurs at a depth <35 cm in the CIOB sediments irrespective of the sedimentation rates (Iyer et al

1997, 1999; Pattan et al 2009; Prasad et al 2007; Pattan 2010; Mascarenhas-Pereira et al 2016). In Figure 3, we have correlated the YTT layer to Layer A from Site 758 based on the sedimentation rates, chemical composition, and morphology. Beginning with the northernmost core, we now detail the SRH present in the four cores.

Core AAS-22/8: In the core AAS-22/8, we have identified six SRH occurring at depths 135-140, 190-195, 205-210, 430-435, 485-490 and 520-520 cm-bsf. Based on the sedimentation rates, SRH at depth 135-140 cm-bsf corresponds to an age of 0.502-0.520 Ma (mean 0.511 ± 0.008) (Table 4). This age is comparable with the 0.49 to 0.538 Ma age provided by Dehn et al. (1991). Given the low mean error of 0.003 Ma of reported age from ODP Site 758 with that of our derived age it is obvious that this SRH (135-140 cm-bsf) corresponds to the MTT.

There are a few studies that pertain to the MTT which has been well identified as Layer C in Site 758 in the Indian Ocean (Imbrie et al 1984; Chesner 1988; Dehn et al 1991). This Layer C (MTT) that occurs between the $\delta^{18}\text{O}$ stage 13.2 and 14.2 was assigned an age of 0.49 to 0.538 Ma (Chesner 1988; Dehn et al 1991). Because of this, there are no reports of MTT layer in the CIOB so far, and our present finding could be the probable be the first report. Also, the absence of information related to MTT may be due to restricted sampling for sediments, scarcity of long cores (≥ 5 m long) and low sedimentation rates in the CIOB. The occurrence of Layer C (MTT) only in AAS-22/8 supports the fact that during the MTT eruption the volume of the surge was less and this has been reflected in the shard counts (Table 2). The SRH between 190 and 195 cm-bsf (Figure 3) correspond to an age of 0.706-0.725 Ma (mean 0.715 ± 0.008) and could be similar to Layer D (0.731-0.750 Ma) of Site 758. Based on the reported age of ODP Site 758 the error calculated for this layer is 0.025 Ma.

In Site 758, the Layer E occurs in the middle of $\delta^{18}\text{O}$ stage 21 and with an age of 0.775 Ma is closest to the OTT (0.840 ± 0.30 Ma; Diehl et al 1987). Considering the age of microtektites (0.77 Ma) and co-occurring glass shards of 0.77 ± 0.008 Ma age, the OTT (i.e. Layer E) is well-documented in the CIOB cores (Glass and Koeberl, 2006; Prasad et al 2007; Pattan et al 2010; Pearce et al 2014).

The next successive layer in the core AAS-22/8 is at depth 430-435 cm-bsf (Figure 3) corresponds to an age of 1.598-1.617 Ma (mean 1.607 ± 0.008) and can be correlated with Layer G of Site 758 which is 1.596-1.653 Ma (Dehn et al 1991). Considering the ODP Site 758 data the error calculated for this layer is 0.017 Ma.

In addition to the above identified SRH, we observed two more SRH at depths 485-490 and 520-525 cm-bsf (Table 5, Figure 3), and these have ages of 1.802-1.821 (mean 1.812 ± 0.008) and 1.933-1.951 Ma (mean 1.942 ± 0.008), respectively. These SRH have distinct type II morphology of glass shards (Figure 5), unlike the other layers. It was further noted that the ages of these two SRH do not match with those reported for Site 758 (Dehn et al 1991).

Core AAS-22/7: There are two SRH in this core one in the top 5 cm-bsf and the other at depth 220-225 cm-bsf (Table 5; Figure 3). Based on the age of sediments the upper SRH is YTT (0.074 Ma) while the lower SRH, associated with microtektites, has an age of 0.696-0.712 Ma (mean 0.77 ± 0.008) and corresponds to the OTT.

Core AAS-22/5: Three SRH are present at depths of 10-15, 110-115 and 245-250 cm-bsf (Table 5; Figure 3). The upper SRH is the newly found YTT, and the middle SRH is the reported OTT (Prasad et al 2007). The lower SRH (245-250 cm-bsf) (Figure 3) corresponds to an age 1.605-1.675 Ma (mean 1.64 ± 0.035 Ma) and is perhaps equivalent to the Layer G (1.596 to 1.636 Ma) of Site 758 (cf. Dehn et al 1991). The error calculated for this layer based on the reported ages from Site 758 is 0.024 Ma.

Core AAS-22/3: In this core, there are nine SRH at depths of 10-15 (YTT), 60-65 (OTT), 170-175, 285-290, 295-300, 325-330, 335-340, 350-355 and 360-370 cm-bsf (Table 5; Figure 3). Based on the sedimentation rates the SRH occurring at depth 170-175 cm (2.195 to 2.265 Ma with a mean value of 2.23 ± 0.008 Ma) could be correlated to Layer H of Site 758 (cf. Dehn et al 1991). The mean error for this layer is 0.021 Ma for ODP Site 758. While the SRH at depth 285-290 cm (3.795-3.865, mean error 3.83 Ma), 295-300 cm (3.935-4.005 Ma with a mean error 3.97 Ma) and 325-330 cm (4.285-4.355 Ma, mean error 4.32 Ma) could be equivalent to Layer h (3.664-3.666 Ma), Layer I (4.124-4.131 Ma) and Layer J (4.526-4.596) of Dehn et al. (1991), respectively. The errors calculated for layer h (0.16 Ma), layer I (0.15 Ma) and from layer J (0.23 Ma) are based on the reported ages from Site 758.

The SRH that occur at 335-340 cm (4.445-4.515 Ma, mean 4.48 Ma) and 350-355 cm (4.705-4.775 Ma, mean 4.72 Ma) can be correlated with the Layers K (4.666-4.667 Ma) and L (4.759-4.765 Ma) respectively of Site 758 (cf. Dehn et al 1991). The bottom-most SRH occurring at depth 365-370 cm-bsf with an age of 4.915 to 4.985 Ma (mean 4.95 Ma) could be equivalent to the Layer M of Site 758 (5.062-5.063 Ma; Dehn et al 1991). The errors calculated for layer K is (0.07 Ma), layer L (0.02 Ma) and layer M (0.11 Ma).

We note that the time span covered by the other three studied cores (AAS-22/3, AAS-22/5, and AAS-22/8) does not exceed 4 Ma and this fact constrains the identification of comparable layers in the CIOB as found in Site 758. To date, the existence of layers H, h, I, J, K, L, and M, was not identified in the CIOB sediments; this could be due to limitations in the length of so far studied sediment cores and their locations.

The composition of the studied glass shards from the SRH was compared with the equivalent layers reported by earlier workers (Table 5). It is observed that the YTT layer reported by Pattan et al (2010) show similar SiO₂ value (76 wt.%) in the cores AAS-22/3 and AAS-22/7, whereas, in AAS-22/5 SiO₂ shows slightly lower values (74 wt.%). The other oxides are similar to the compared values. Layer C in the core AAS-22/8 was compared with Westgate et al (1988) shows a slightly low SiO₂ value (74 wt.%) along with CaO (0.76 wt.%). On the other hand, K₂O values are observed to be high (4.2 wt.%). The glass shards from Layer D and below are compared with those reported by Dehn et al (1991). Layer D shows lower values in K₂O (2.79 wt.%), CaO (0.14 wt.%), and slightly higher values in FeO (0.9 wt.%) and Al₂O₃ (12.32 wt.%) compared to the reported values. The Layer E (OTT) is confirmed by the co-occurrence of microtektites and composition of the shards with the earlier identified layers, show a similar trend. In Layer G, the SiO₂ value is similar (73-74 wt.%) to the reported values (73 wt.%) (Table 6). The layer at depth 245-250 cm in core AAS-22/5 shows slightly higher values in CaO (1.01 wt.%), MgO (0.14 wt.%) and Al₂O₃ (11.97 wt.%), while K₂O shows a slightly lower value (3.17 wt.%). Layers H, h, and I have values nearly similar to the reported site, while layers J, K, L, and M show about 1% higher SiO₂ values compared to the reported ones. On the other hand, the TiO₂, Na₂O, and CaO show a slightly lower value compared to the ODP Site 758 but overall, the studied shards depict a good similarity with the reported values by other workers.

5.3 Source and Formation of glass shards: Since more than a couple of decades, the source of glass shards present in the CIOB has been controversial. There are two schools of thoughts: (i) the cusped glass shards belong to the YTT (Pattan et al 1999), except in some cases wherein the glass shards are of the OTT (Glass and Koeberl 2006; Pattan et al 2010), while (ii) blocky shards resulted in intraplate volcanism in the CIOB (Iyer et al 1997; Mascarenhas-Pereira et al 2016). Mascarenhas-Pereira et al (2006) examined the likely sources for the CIOB glass shards by comparing these with those that originated from the neighbouring terrestrial volcanoes. Based on the chemical composition of the CIOB glass shards (Tables 3 and 5), the volcanic sources such as the Reunion hotspot, Kerguelen plume,

Broken Ridge, Afro-Arabian flood volcanic, and Taupo volcanic centre were ruled out. This is because these sources have also contributed basaltic materials, and the ages of the shards do not correlate with those from the terrestrial sources. Considering these reports and our present observations, we suggest that the shards occurring in shallow depths within the four sediment cores are mainly the YTT, while those at deeper depths are either from earlier eruptions of Toba and/or were formed in-situ.

In recent years, there has been growing evidence of pyroclastic eruptions in the deep-sea environment, and various models have been developed to understand their mechanism of formation (Clague et al 2003, 2009; Helo et al 2008, 2011). These submarine eruptions of strombolian style are known to transfer gases directly to the cold surrounding deep waters resulting in pyroclastic deposits (Head and Wilson, 2003). The fragmentation of pyroclasts in the deep-sea could be driven by the release of CO₂ (Helo et al 2013) and this fact indicates that pyroclastic fragments deposited at abyssal depths are independent of their source and types of origin. The bubble wall glass shards are known to have a hydrovolcanic origin (Schipper and White 2010), and the process is well identified in the sub-aqueous environment. In contrast, blocky glass shards devoid of vesicles (cf. Figure 3B) are the products of a rapid interaction of lava and seawater during phreatomagmatic eruptions (Maicher and White 2001). On the other hand, Fisher and Schmincke (1984) suggested that glass shards with curved surfaces, three bubble wall junctions or double concave morphology result from an explosive volcanic eruption.

It is noteworthy that an analogous observation was made of glass morphology and chemistry in the four short cores (max. 40 cm) recovered from the CIOB. The SRH in these cores were reportedly formed by hydrovolcanic activities that occurred during 85, 107-109, and 142-146 ka ago and a crypto-tephra layer of 34 ka (Mascarenhas-Pereira et al 2016). Considering the above facts, we find that although the products of Toba (especially YTT) may be common in the CIOB sediments, the possibility of an intra-basinal origin of glass shards cannot be ruled out especially for those SRH that cannot be correlated with the well-established layers present in Site 758.

6.0 Discussion

Morphology, size, and distribution of volcanic pyroclasts such as glass shards and their deposition in a submarine environment can be used as tools to understand the volcanic cyclicality, type of eruption and intensity. The distribution of the glass shards is dependent on

the volume of the volcanic surge and extent of its lateral spread. Morphology is another characteristic of glass shard, with the shape being an indicator of the type of eruption (aerial or submarine) and the size could also help to understand the distance of travel of the tephra fallout. In the present study, we have used morphology, size and major oxide chemical composition of the glass shard to decipher their distribution in the undisturbed sediments cores of the CIOB. Further, we have compared our results with the SRH identified in Site 758.

Site 758 is considered as a repository for glass shards that are derived from the IVA. To-date, 15 layers i.e. Layers A to M, d and h (Dehn et al 1991), and another layer of 8 Ma (Padmakumari and Ahmad 2004; Jumaila et al 2017), give an insight to the cyclic volcanism that has occurred over millions of years. It is significant that irrespective of the depth of occurrence the glass shards are silicic in composition and have a distinct morphology such as cusped and Y-shaped intersections (Figure 4). So far, only two layers (i.e. YTT and OTT) of the total of 16 layers have been reported to occur in the CIOB (Iyer et al 1997; Pattan et al 1999, 2010; Pearce et al 2014). Based on our present observation, it is evident that the YTT shards are confined up to a core depth of <35 cm irrespective of the rate of sedimentation in the basin. This observation is consistent with the earlier studies (Table 1).

The CIOB seafloor is supposedly carpeted largely by the YTT, but we did not encounter this layer in the sub-surface sediment of core AAS-22/8 (Table 5; Figure 3). We ascribe the absence of YTT to the erosion of sediments by the Antarctica Bottom Watermass (AABW) that pass through the basin (Laverigne et al 2017). This is corroborated by the absence of the radiolarian species *Collosphaera invaginate* from the CIOB surface sediments (Johnson and Nigrini 1982; Banakar et al 1991). Additionally, the AABW currents also led to rolling and smoothing of FeMn nodules lying on the surface of the CIOB sediments near the 79° E FZ (Vineesh et al 2009).

Apart from the YTT and OTT, there are no other reports of Toba tephra in the CIOB. The present study has helped to reveal for the first time the existence of other Toba eruptives. The identified SRH from all the four cores have been compared based on chemistry, and morphology with the 16 reported layers (Table 5) identified in Site 758. The chemical composition of the shards shows high SiO₂ (73 to 75 wt.%) and high total alkali (Na₂O+K₂O ~5 wt.%) which are typical for the Toba eruptives that are rhyolitic in composition as is attested by the TAS diagram (Figure 5). The present work indicates a bimodal morphology of

the glass shards in the CIOB. Similarly, size analysis carried out for glass shards from all the identified SRH indicates the shards to range from 30 to 720 μm .

The identified SRH in the northernmost core AAS-22/8, i.e. Layer C (MTT) and Layer D have a significantly lower count of glass shards compared to the OTT layer (Figure 3). We ascribe the presence of these two layers to the proximity of the cores to the IVA source and the enhanced volcanic surge output. The reasons for the absence of layer D in the other three cores could be due to its deposition soon after the eruption of OTT (0.840 ± 0.30) in a short interval of time along with low volume of volcanic surge. Thus, it is believed that some of these layers may have been mixed and therefore are not traceable in the CIOB sediment cores (Pattan et al 2010).

The OTT (layer E) in the present study occurs with microtektites (age 0.77 Ma) at depth 205-210 cm-bsf (AAS 22/8), 220-225 (AAS 22/7), 110-115 (AAS 22/5) and 60-65 (AAS 22/3). The OTT has been well documented in the sediment cores from the CIOB by several workers (Glass and Koeberl 2006; Prasad et al 2007; Pattan et al 2010; Pearce et al 2014).

In Site 758 the Layer F occurs between $\delta^{18}\text{O}$ stage 45 and 46, which corresponds to 1.273 and 1.294 Ma (Dehn et al 1991). Similarly, an age of 1.2 ± 0.16 Ma was determined using fission-track method (Nishimura et al 1977). These ages match well with the HDT of the IVA. In all our four cores, we did not encounter any SRH at depth (Figure 3) that coincides with this age. This suggests that the HDT layer may not have been preserved or the ash fallout of the HDT perhaps did not reach the CIOB seafloor due to the very less volume of surge generated during the volcanic eruption (Chesner and Rose 1991). Interestingly, some of the FeMn oxides-coated pumice in the CIOB are the HDT products of 1.2 Ma (Kalangutkar et al 2011; 2015).

The SRH at depths of 430-435 (AAS-22/8) and 245-250 (AAS-22/5) are related to Layer G of Site 758. The likely reasons for the absence of Layer G in AAS-22/7 could be due to the high sedimentation rate of 3.1 mm/ka and the limiting age of 1.74 Ma for this 5.5 m long core. We did not observe Layer G in the southernmost core AAS-22/3. The possible reason for the absence of Layer G could be the location of this core (17°S) far from the IVA source.

We further find that though all the four cores are nearly 5m long, the northern two cores have maximum ages of 2.08 Ma (AAS-22/8) and 1.74 Ma (AAS-22/7) compared to the southern cores that are of 3.49 Ma (AAS-22/5) and 7.79 Ma (AAS-22/3) ages. This fact suggests that the northern part of the study area witnesses higher sedimentation input, thereby

making it difficult to identify layers H to M that are older than the age of the core. On the other hand, the southern cores with low sedimentation rates have a better probability of occurrence of the other layers as found in Site 758 (Dehn et al 1991).

The SRH at depths 170-175 cm (2.195-2.265 Ma, mean 2.23 Ma) and 285-290 cm (3.795-3.865, mean 3.83 Ma) are comparable with Layer H (2.238-2.265 Ma) and Layer h (3.664-3.666) of Site 758. Similarly, the SRH at depth 295-300 cm-bsf (3.935-4.005 Ma, mean 3.97 Ma) could be well-correlated with Layer I (4.124-4.131 Ma), and the SRH at depth 325-330 cm-bsf (4.285-4.355 Ma, mean 4.32 Ma) is equivalent to Layer J (4.552-4.560 Ma). The next well preserved SRH identified at depth 335-340 cm-bsf (4.445-4.515 Ma, mean 4.48 Ma) correlates with Layer K (4.666-4.667 Ma). The oldest two layers at depth 350-355 cm-bsf (4.705-4.775 Ma, mean 4.74 Ma) and 365-370 cm-bsf (4.915-4.985 Ma, mean 4.95 Ma) could be correlated with Layers L (4.759-4.765) and M (5.062-5.063 Ma) respectively of Dehn et al (1991).

The identified rhyolitic glass shards from the present study with type I morphology were evaluated compositionally with their equivalents occurring in the Indian Ocean (Table 5). The SRH in the upper section of the cores were compared with an average of 92 YTT shards reported by Pattan et al. (1992). Though the reports about the occurrence of the MTT are very few, the SRH layer identified as MTT was further compared with an average of 18 shards reported by Westgate et al (1988). Similarly, the OTT shards were compared with an average of 19 glass shards reported by Pattan et al. (2010) while the shards in Layers D, and G to M were appraised with those reported by Dehn et al (1991) from ODP Site 758. The chemical composition of the referenced tephra layers (Table 5) corroborates with the layers identified using sedimentation rates and microtektites. The reference data when plotted in the TAS diagram (Figure 5) also signifies a similar composition.

The two SRH at depths of 485-490 and 520-525 cm-bsf in the core AAS-22/8 have glass shards of type II morphology and are 1.802-1.821 and 1.933-1.951 Ma, respectively. Though these glass shards were abundant (2,972 shards in 430-435 cm and 2,586 shards in 520-525 cm), rhyolitic in composition with high SiO₂ (73 to 74 wt.%) and similar to the Indonesian glass shards but they do not correlate with those from for Site 758 (Dehn et al 1991). The shape of the glass shards is directly related to the mode of formation (Wohletz 1983). The vesicular glass shards with cusped and Y-shaped intersections morphology are indicative of sub-aerial eruptions; while the blocky glass shards with scarce vesicles are known to form due to hydroclastic processes (Fisher and Schmincke 1984; Helo et al 2013).

The blocky glass shards, in the two above mentioned SRH with a smooth surface are poorly vesiculated and were perhaps formed from intraplate volcanism in the CIOB. The non-vesicular nature of these shards suggests that they were formed under high hydrostatic pressure from a silicic melt during a phase of a localized strombolian event. Our findings corroborate that of Mascarenhas-Pereira et al (2016) who also reported similar type II glass shards and had proposed in-situ origin for some of the SRH in the CIOB.

7.0 Conclusions

An investigation of four long sediment cores (average length 5m) that were retrieved along the transect line located in the north (7°S) to the south (17°S) reveals the occurrence of multiple shard-rich horizons (SRH). These SRH helped to provide the first detailed tephrochronology for the volcanic glass shards identified in the CIOB sediments

Sedimentation rate derived using the abundance peak of Australasian microtektites (age 0.77 Ma), suggest variations across the basin with the highest rate (3.1 mm/ka) observed in the north part of the study area while the rates were extremely low (0.718 mm/ka) in the southern part of the basin. The estimated sedimentation rates are also well correlated with ages derived by other workers and fit extremely well with those reported for ODP Leg 21 Site 758 that were dated using paleomagnetic and $\delta^{18}\text{O}$ methods.

Based on our comparative study of surface sediments floored with the YTT, we find that irrespective of the rate of sedimentation, the YTT in the basin is restricted to a depth of <35 cm-bsf. Furthermore, we identified two layers (MTT = Layer C), and D) that occur between the ubiquitous YTT and OTT (Layer E) and ten layers (G, H, h, I, J, K, L, M and two of in-situ source) occurring below the OTT.

The two unknown SRH that are present between layer G and H were compositionally similar to that of Toba shards but their morphology differs which provides supporting confirmation of their localized in-situ phreatomagmatic origin during short volcanic episodes within the basin. Further work would help to understand the mechanism of deep-sea silicic volcanism not only in the CIOB but also in the other oceans.

Acknowledgements

We acknowledge the Director of CSIR-NIO, Goa for providing facilities to carry out the study. We thank Dr. Martin Jutzeler, University of Tasmania for his invaluable suggestions on an earlier version of the manuscript. We are grateful to Mr. V. Khedekar, Ms. Sahina and Ms. Valency for assisting during the SEM-EDS analysis and to Mrs. Charushila

and Mr. V. Gaikwad for helping in preparing Figures 1 and 3. AA thanks CSIR (Direct SRF) and the project “Surveys for Polymetallic Nodules” (GAP 2175) for the research funds. We profusely thank the two anonymous reviewers for valuable comments which helped us to improve the manuscript. We are grateful to the Editor-in-Chief, Dr. N. V. Chalapathi Rao, for encouraging us to submit the revised manuscript. We appreciate the help rendered by the Captain, crew, and participants of the AAS-22 cruise during sediment coring operations. This is NIO’s contribution number -----.

References

- Acharyya S K and Basu P K 1993 Toba ash on the Indian subcontinent and its implications for the correlation of late Pleistocene alluvium; *Quat. Res.* 40 10–19.
- Amonkar A and Iyer S D 2017 An account of silicic glass shards in the Central Indian Ocean Basin: terrestrial and in-situ origin; (Abstract) OSICON-17 ESSO-NCESS Thiruvananthapuram Kerala India.
- Banakar V K Gupta S M and Padmavathi V K 1991 Abyssal sediment erosion in the Central Indian Basin: Evidence from radiochemical and radiolarian studies; *Mar. Geol.* 96 167-173.
- Banerjee B Ahmad S M Babu E V S S K Padmakumari V M Beja K S Satyanarayanan M Krishna A K 2019. Geochemical and isotopic study of southern Bay of Bengal sediments: Implications for provenance and paleoenvironment during the middle Miocene. *Paleoeco. Palaeoclim. Palaeoeco.* 514 156-167.
- Borole D V 1993 Late Pleistocene sedimentation: A case study of the central Indian Ocean Basin; *Deep-Sea Res.* 40 761-775.
- Bühring C and Sarnthein M 2000 Toba ash layers in the South China Sea: evidence of contrasting wind directions during eruption ca. 74 ka *Geol.* 28 275-278.
- Chesner C A and Rose W I 1991 Stratigraphy of the Toba Tuffs and the evolution of the Toba Caldera Complex, Sumatra, Indonesia; *Bull. Volcanol.* 53 343–356.
- Chesner C A Rose W I Deino A Drake R and Westgate J A 1991 Eruptive history of Earth’s largest Quaternary caldera (Toba, Indonesia) clarified; *Geol.* 19 200–203.
- Chesner C A 1998 Petrogenesis of the Toba Tuffs, Sumatra, Indonesia; *J. Petrol.* 39 397–438.
- Clague D A Davis A S and Dixon J E 2003 Submarine Strombolian eruptions on the Gorda mid-ocean ridge; *Explosive Subaqueous Volcanism. Geophys. Monogr. Ser.* 140 111–128.
- Clague D A Paduan J B and Davis A S 2009 Widespread strombolian eruptions of mid-ocean ridge basalt; *J. Volcanol. Geotherm. Res.* 180 171-188.
- Costa A Smith V C Macedonio G and Matthews N E The magnitude and impact of the Youngest Toba Tuff super-eruption; *Front. Earth Sci.* 2, 1-8.
- Das P Iyer S D Kodagali V N and Krishna, KS 2005 Distribution and origin of seamounts in the Central Indian Ocean Basin; *Mar. Geod.* 28 259-269.

- Das P Iyer S D and Kodagali V N 2007 Morphological characteristics and emplacement mechanism of the seamounts in the Central Indian Ocean Basin; *Tectonophy.* 443 1-18.
- de Lavergne C Madec G Roguet F Holmes R M and McDougall T J 2017 Abyssal Ocean overturning shaped by seafloor distribution; *Nature* 551 181–186.
- Dehn J Farrel J W and Schmincke H -U 1991 Neogene tephrochronology from ODP Site 758 on Ninety East Ridge: Indonesian arc volcanism of the past 5 Ma; *Proceedings of ocean drilling program Sci. Res.* 121 273–295.
- Diehl J F Onstott T C Chesner C A and Knight M D 1987 No short reversals of Brunhes age recorded in the Toba Tuffs, north Sumatra, Indonesia; *Geophys. Res. Lett.* 14 753–756.
- Fisher R V and Schmincke H -U 1984 *Pyroclastic Rocks*; Springer, 472.
- Gasparotto G Spadafora G Summa V and Tateo F 2000 Contribution of grain size and compositional data from the Bengal Fan sediment to the understanding of Toba volcanic event; *Mar. Geol.* 162 561-572.
- Gathorne-Hardy F J and Harcourt-Smith W E H 2003 The super-eruption of Toba, did it cause a human bottleneck?; *J Human Evol.* 45 227–230.
- Gatti E Mokhtar S Talib K Rashidi A Gibbard P Oppenheimer C 2012. Depositional processes of reworked tephra from the Late Pleistocene Younger Toba Tuff deposits in the Lenggong Valley, Malaysia, *Quat. Res.* 79 228-241.
- Glass B P and Koeberl C 2006 Australasian microtektites and associated impact ejecta in the South China Sea and the middle Pleistocene supereruption of Toba; *Meteorit. Planet. Sci.* 41 305–326.
- Goldberg E D and Koide M 1963 Rates of sediment accumulation in the Indian Ocean; *Earth Sci. and Meteo.* 90-102.
- Gourlan A T Meynadier L Allegre C 2008 Tectonically driven changes in the Indian Ocean circulation over the last 25 Ma: Neodymium isotope evidence; *Earth and Planetary Sci. let.* 267 353-364.
- Gupta S M 1988 Radiolarian zonation and volcanic ash-layers in two Quaternary sediment cores from the Central Indian Basin; *J. Palaeontol. Soc. India* 33 59–71.
- Gupta S M 1991 New ichthyoliths from ferromanganese crusts and nodules from the Central Indian Ocean Basin; *Micropaleont.* 37 125–147.
- Gupta S M Fernandes AA and Mohan R 1996 Tropical sea surface temperatures and the Earth's eccentricity cycles; *Geophys. Res. Lett.* 23 3159–3162.
- Gupta S M 2009 Radiolarian abundance - a monsoon proxy responding to the Earth's orbital forcing: Inferences on the mid-Brunhes climate shift; *Earth Sci. India* 2 1-8.
- Head J W I and Wilson L 2003 Deep submarine pyroclastic eruptions: theory and predicted landforms and deposits; *J. Volcanol. Geotherm. Res.* 121 155–193.
- Helo C Clague D A Dingwell D B and Stix J 2013 High and highly variable cooling rates during pyroclastic eruptions on Axial Seamount, Juan de Fuca Ridge; *J. Volcanol. Geotherm. Res.* 253 54–64.
- Helo C Clague D A and J Stix 2008 Pyroclastic eruptions from axial caldera, Juan de Fuca Ridge, NE Pacific Ocean; *IOP Conf. Ser.* 3 012005.

- Helo C Longpre M –A Shimizu N Clague DA Stix J 2011 CO₂ rich magmas from Axial Seamount – A link to explosive eruptions on mid-ocean ridges?; *Nature Geosci* 4 260-263.
- Imbrie J Hays J D Martinson D G McIntyre A Mix A C Morley J J Pisias N G Prell W L and Shackleton N J 1984 The orbital theory of Pleistocene climate support from a revised chronology of the marine delta δ¹⁸O record; In Berger, A Imbrie, J Hays, J Kukla, G and Saltzman, B. (Eds.), *Milankovitch and Climate* (pt. 1): Dordrecht (D. Reidel), 269-305.
- Iyer S D 2007 Volcanics of the Central Indian Ocean Basin; *J. Geol. Soc. India*, 70 883-884.
- Iyer S D Shyam P M Gupta S M and Charan S N 1997 Evidence for recent hydrothermal activity in the Central Indian Basin; *Deep-sea Res.* 44 1167–1184.
- Iyer S D Fernandes G Q and Mahender K 2012 Coarse fraction components in a red-clay sediment core, Central Indian Ocean Basin: their occurrence and significance; *J. Ind. Assoc. Sed.* 31 123-135.
- Jarosewich E Nelen J A and Norberg J A 1980 Reference samples for electron microprobe analysis; *Geostd. Newslet.* 4 43–47.
- Johnson D A and Nigrini C 1982. Radiolarian biogeography in the surface sediments of Eastern Indian Ocean; *Mar. Micropaleontol.* 7 237-282.
- Jumaila C P U Pattan J N Ahmad S M Parthiban G Khedekar V D Padmakumari V M and Milindraj P 2017 Morphology and chemical composition of ash layer of about 8 Ma old from ODP-758 site Bay of Bengal; *Ind. J. Geo-Mar. Sci.* 46 871–876.
- Kalangutkar N G Iyer S D Mascarenhas-Pereira M B L and Nath B N 2015 Hydrothermal signature in ferromanganese oxide coatings on pumice from the Central Indian Ocean Basin; *Geo-Mar. Lett.* 35 221–235.
- Kalangutkar N G Iyer S D and Ilangovan D 2011 Physical properties, morphology and petrological characteristics of pumices from the Central Indian Ocean Basin; *Acta Geol. Sinc.* 85 826-839.
- Kennet J P 1981 Marine tephrochronology, In: *The Sea*; 7 1373–1436.
- Knight M D Walker G L Ellwood B B and Diehl J F 1986 Stratigraphy paleomagnetism, and magnetic fabric of the Toba tuffs: Constraints On the sources and eruptive styles; *J. Geophys. Res.* 91 10355-10382.
- Kolla V and Kidd R 1982. Sedimentation and sedimentary processes in the Indian Ocean; *The Ocean Basins and Margins, The Indian Ocean.* Plenum. 6 1-45.
- Kunz J Bollinger K Jessberger E K and Storzer D 2000 Ages of Australasian tektites; *Lunar Planet. Sci.* 36 809–810.
- Lane C S Blockley S P Mangerud J Smith V C Lohne O S Tomlinson E Matthews I P and Lotter A 2012 Was the 12.1 ka Icelandic Vedde ash one of a kind?; *Quat. Sci. Rev.* 33 87-99.
- Lane C S Lowe D J Blockley S P E Suzuki T and Smith V C 2017 Advancing tephrochronology as a global dating tool: Applications in volcanology, archaeology, and palaeoclimatic research; *Quat. Geochron.* 40 1–7.
- Lee M Y Chen C H Wei K Y and Iizuka Y 2003 Astronomical calibration of the first Toba super-eruption from deep-sea sediments; *Geophys. Res.* 5 12799.
- Lee M Y Chen C H Wei K Y Iizuka Y and Carey S 2004 First Toba super-eruption revival; *Geol.* 32 61–64.

Liu Z Colin C and Trentesaux A 2006 Major element geochemistry of glass shards and minerals of the Youngest Toba Tephra in the southwestern South China Sea; *J. Asian Earth Sci.* 27 99–107.

Lowe D J 2011 Tephrochronology and its applications: A review; *Quart. Geochron.* 6 107-153.

Mark D F Petraglia M Smith V C Morgan L E Barfod D N Ellis B E Pearce N J Pal J N and Korisettar R 2014 A high-precision $^{40}\text{Ar}/^{39}\text{Ar}$ age for the Young Toba Tuff and dating of ultra-distal tephra: forcing of quaternary climate and implications for hominin occupation of India; *Quat. Geochronol.* 21 90–103.

Mark D F Renne P R Dymock R C Smith V C Simon J I Morgan L E Staff R A Ellis B S and Pearce N J 2017 High-precision $^{40}\text{Ar}/^{39}\text{Ar}$ dating of Pleistocene tuffs and temporal anchoring of the Matuyama-Brunhes boundary; *Quat. Geochronol.* 39 1-23.

Martin-Barajas A and Lallier –Verges E 1993 Ash layers and pumice in the Central Indian Basin: relationship to the formation of manganese nodules; *Mar. Geol.* 115 307–329.

Mascarenhas–Pereira MBL Nath B N Borole DV and Gupta S M 2006 Nature, source and composition of volcanic ash in sediments from a fracture zone trace of Rodriguez Triple Junction in the Central Indian Basin; *Mar. Geol.* 229 79–90.

Mascarenhas–Pereira M B L Nath B N Iyer S D Borole D V Parthiban G Jijin R and Khedekar V 2016 Multiple ash layers in late Quaternary sediments from the Central Indian Basin; *J. Volcano. Geotherm. Res.* 316 85-100.

Maicher D and White J D L 2001. The formation of deep-sea Limu o Pele; *Bull. Volcanol.* 63 482–496.

Mukhopadhyay R Ghosh A K, and Iyer S D 2018 The Indian Ocean nodule field: Geology and Resource Potential; 2nd edition 413.

Nath B N Rao V P C and Becker K P 1989 Geochemical evidence of terrigenous influence in deep-sea sediments up to 8°S in the Central Indian Basin; *Mar. Geol.* 87301–313.

Nath B N 2001 Geochemistry of sediments; *The Indian Ocean: A perspective.* 2 645–689.

Nath B N Sijinkumar A V Borole D V Gupta S M Mergulhao L P Mascarenhas-Pereira M B L Ramaswamy V Gupta M V S Possnert G Aldahan A Khadge N H and Sharma R 2013 Record of carbonate preservation and the Mid-Brunhes climatic shift from a seamount top with low sedimentation rates in the Central Indian Basin; *Boreas* 42 762–778.

Ninkovitch D 1979 Distribution, age and chemical composition of tephra layers in the deep-sea sediments off western Indonesia; *J. Volcanol. Geotherm. Res.* 5 67–86.

Nishimura S Abe E Yokoyama T Wirasantosa S and Dharma A D 1977 Danau Toba—the outline of Lake Toba, North Sumatra, Indonesia; *Paleolimnology Lake Biwa, and the Jap. Pleist.* 5 313–332.

Oppenheimer C 2002 Limited global change due to the largest known Quaternary eruption Toba ~74 kyr BP ?; *Quat. Sci. Rev.* 21 1593–1609.

Padmakumari V M and Ahmad S M 2004 Ash layer at ~8 Ma in ODP Site 758 from the Bay of Bengal: evidence from Sr, Nd isotopic compositions and rare earth elements; *Curr. Sci.* 86 1323–1325.

Pattan J N Shane P and Banakar V K 1999 New occurrence of Youngest Toba Tuff in abyssal sediments of the Central Indian Basin; *Mar. Geol.* 155 243–248.

- Pattan J N and Parthiban G 2007 Do manganese nodules grow or dissolve after burial? Results from the Central Indian Ocean Basin; *J. Asian Earth Sci.* 30 696–705.
- Pattan J N Shane P A R Pearce N J G Banakar V K and Parthiban G 2002 An occurrence of the 74 ka Youngest Toba Tephra from the western continental margin of India; *Curr. Sci.* 80 1322–1326.
- Pattan J N Shyam P M and Babu E V S S K 2010. Correlation of the Oldest Toba Tuff to sediments in the central Indian Ocean Basin; *J. Earth Syst. Sci* 119 531–539.
- Pearce N J Westgate J A Gatti E Pattan J N Parthiban G and Achyuthan H 2014 Individual glass shard trace element analyses confirm that all known Toba tephra reported from India is from the c. 75-ka Youngest Toba eruption; *J. Quat. Sci.* 29 729–734.
- Prasad M S Mahale V P and Kodagali V N 2007 New sites of Australasian microtektites in the central Indian Ocean: implications for the location and size of source crater; *J. Geophys. Res. (Oceans)* 112 1-11.
- Prasad M S Roy S K and Gupta A 2010 Changes in abundance and nature of micro impact craters on the surfaces of Australasian microtektites with distance from the proposed source crater location; *Meteor. Planet. Sci.* 45 990–1006.
- Prasad M S Rudraswami N G and Panda D K 2013 Micrometeorite flux on Earth during the last ~50,000 years; *J. Geophys. Res. (Planets)* 118 1–19.
- Rampino M R and Self S 1993 Bottleneck in human evolution and the Toba eruption; *Science* 262 1955.
- Rose W I and Chesner C A 1987 Dispersal of ash in the great Toba eruption, 75 ka; *Geology* 15 913–917.
- Schipper C I and White J D L 2010 No depth limit to hydrovolcanic Limu o Pele: analysis of Limu from Loihi Seamount Hawaii; *Bull. Volcanol.* 72 149–164.
- Schultz H Emeis K Erlenkeuser H von Rad U and Rolf C 2002 The Toba volcanic event and interstadial/stadial climates at the Marine Isotope Stage 5/4 transition in the northern Indian Ocean; *Quat. Res.* 57 22–31.
- Scudder R P Murray R and Plank T 2009 Dispersed ash in deeply buried sediment from the Northwest Pacific Ocean: an example from the Izu-Bonin arc (ODP site 1149); *Earth Planet. Sci. Lett.* 284 639–648.
- Scudder R P Murray R W Schindlbeck J C Kutterolf S Hauff F Underwood M B Gwizd S Lauzon R and McKinley C C 2016 Geochemical approaches to the quantification of dispersed volcanic ash in marine sediment; *Prog. Earth Planet. Sci.* 3 1-32.
- Shane P Westgate J Williams M and Korisettar R 1995 New geochemical evidence for the youngest Toba Tuff in India; *Quat. Res.* 44 200–204.
- Song S R Chen C H Lee M Y Yang T F Iizuka Y and Wei K Y 2000 Newly discovered eastern dispersal of the youngest Toba Tuff; *Mar. Geol.* 167 303–312.
- Srivastava A K and Singh A 2019 YTT ash from Quaternary sediments of Kapileshwar area, Purna alluvial basin, Central India; *Quater. Int.* doi.org/10.1016/j.quaint.2019.02.006
- Storey M Roberts R G and Saidin M 2012 Astronomically calibrated Ar-40/Ar-39 age for the Toba supereruption and global synchronization of late Quaternary records; *Proc. Natl. Acad. Sci. USA* 109 (46)18684-18688.

- Sukumaran N P Banerjee R Borole D V and Gupta S M 1999 Some aspects of volcanic ash layers in the Central Indian Basin *Geo-Mar. Lett.* 18 203–298.
- Udinstev G B 1975 *Geological-Geophysical Atlas of the Indian Ocean*; Pergamon London 151.
- Vineesh T C Nath B N Banerjee R Jaisankar S and Lekshmi V 2009 Manganese nodule morphology as indicators for oceanic processes in the Central Indian Basin *Inter. Geol. Rev.* 51 27-44.
- Weisner M Wang Y and Zheng L 1995 Fallout of volcanic ash to the deep South China Sea induced by the 1991 eruption of Mount Pinatubo, Philippines; *Geology* 23 885–888.
- Westgate J A Shane P A R Pearce N J G Perkins W T Korisetar R Chesner C A Williams M A J Acharyya S K 1998 Toba Tephra across India; *PANGAEA*, doi.org/10.1594/PANGAEA.754857.
- Williams M A J Ambrose S H van der Kaar S Ruehleemann U Chattopadhyaya J P and Chauhan P 2009 Environmental impact of the 73 ka Toba super-eruption in South Asia; *Palaeogeogr. Palaeoclim, Palaeoeco.* 284 295–314.
- Wittke J H James C W Ted E B James P K Douglas J K Moore M T Gordon C. H, Kenneth B T Albert C G Christopher R M Daniel I R Ray J H Lopinot N H Ferraro D I srade-Alcántara I Bischoff J L De Carli P S Hermes R E Kloosterman J B Revay Z Howard G A Kimbel D R Kletetschka G Nabelek L Lipo C P Sakai S West A Firestone R B 2013. Evidence for deposition of 10 million tonnes of impact spherules across four continents 12,800 y ago; *Proc Natl Acad Sci U S A.* 110(23), E2088–E2097.
- Wohletz K H 1983 Mechanisms of hydrovolcanic pyroclast formation: size, shape, and experimental studies; *J. Volcanol. Geotherm. Res.* 17 31–63.

Table 1: Details of the studied cores and compilation of reported glass shards occurring in the Central Indian Ocean Basin.

Sr No.	Sediment core	Latitude (°S)	Longitude (°E)	Water Depth (m)	Core recovery length (cm)	Reported depth of shards	References
1	AAS-22/8	7° 05.289	78° 07.712	5180	560	205-210 (OTT)	Present study, Prasad et al (2007), Pearce et al (2014)
2	AAS-22/7	10° 00.988	78° 08.971	5240	550	0-5 (YTT) 220-225 (OTT)	Present work
3	AAS-22/5	15° 06.619	78° 11.742	5030	490	10-15 (YTT) 115-120 (OTT)	Present study, Prasad et al (2007), Pearce et al (2014)
4	AAS-22/3	16° 59.590	77° 59.665	4760	560	10-15 (YTT) 60-65 (OTT)	Present study, Prasad et al (2007), Pattan et al (2010), Pearce et al (2014)
5	NR-1	9° 99.00	77° 92.00	5250	28	0-10 (YTT)	Banakar et al (1991), Pattan et al (2002)
6	NR-35	11.56°	78.49°	5450	23.5	14-26 (YTT)	Banakar et al (1991), Pattan et al (2002)
7	NR-21	11.30°	78.49°	5325	32	20-30 (YTT)	Banakar et al (1991), Pattan et al (2002)
8	NR-54	7°	78.15°	5200	70	30-35 (YTT)	Pattan et al (2002)
9	SK-226	13.08°	75.00°	5270	36	18-26 (YTT)	Pattan et al (2002)
10	SS-657	14.00°	76.00°	5050	36	6-14 (YTT)	Pattan et al (2002)
11	AAS-38/2	8° 29.868	77° 59.761	5438	na	185-190 (OTT)	Prasad et al (2007), Pearce et al (2014)
12	AAS-V/GC-02	13° 01.48	75° 27.04	5099	na	165-170 (OTT)	Pattan et al (2010), Pearce et al (2014)
13	BC-14	14° 00.231	75° 30.064	5145	26	18-20 (YTT) 22-24 (85 ka)* 8-10 (34 ka)**	Mascarenhas-Pereira et al (2016)
14	BC-20	12° 00.066	75° 29.893	5200	34	16-18 (YTT) 24-26 (107-109 ka)* 32-34 (141-146 ka)*	Mascarenhas-Pereira et al (2016)
15	BC-25	10° 59.964	75° 29.927	5300	34	16-18 (YTT), 24-26 (107-109 ka)* 32-34 (141-146 ka)*	Mascarenhas-Pereira et al (2016)

The details of the four gravity cores used in the present study are presented in serial numbers 1 to 4. Legends: * = shards occurring in these horizons were reported to be of intra basinal origin derived by submarine hydrovolcanic activity, ** = Cryptotephra deposit of 34 ka, YTT = Youngest Toba Tuff (74 ka), OTT = Oldest Toba Tuff (0.84 Ma). na = not available.

Table 2: Components occurring in the > 63 µm coarse fraction from the studied core is listed below. Only those depths have been reported/described where the glass shards were abundant. The components are listed in descending order of abundance. The shard counts are calculated per 0.1mg of the CF.

Core	Depth	Counts	Microscopic Description
AAS-22/8	135-140	2133	Radiolarians, glass shards, micronodules (few).
	190-195	3482	Glass shards, radiolarians.
	205-210	4607	Glass shards, radiolarians, tektites.
	430-435	2972	Radiolarians, glass shards.
	485-490	2586	Radiolarians, glass shards.
	520-525	3507	Glass shards, radiolarians.
AAS-22/7	0-5	4593	Radiolarians, glass shards, micronodules, bread crust, magnetite spherules.
	220-225	4170	Radiolarians, glass shards, micronodules, basaltic pieces, tektites.
AAS-22/5	10-15	3044	Radiolarians, glass shards, micronodules (few).
	110-115	2915	Radiolarians, glass shards, micronodules, tektites.
	245-250	1690	Glass shards, palagonite, and micronodules (few).
AAS-22/3	10 -15	4973	Glass shards, radiolarians, micronodules (few).
	60-65	3322	Glass shards, radiolarians, tektites, Fe-coated rock pieces (few).
	170-175	2025	Glass shards, palagonite, micronodules, biota, shark teeth (few).
	285-290	1600	Glass shards, micronodules, palagonite, biota (strings).
	295-300	3214	Glass shards, radiolarians (milky white), micronodules, palagonite grains.
	325-330	2800	Glass shards, palagonites.
	335-340	1882	Glass shards, micronodules, palagonite, shark tooth.
	350-355	2153	Glass shards, palagonite, micronodules, shark tooth.
	365-370	2100	Glass shards, palagonite, and micronodules (few).

Table 3: Chemical composition (wt. %) of the glass shards (EPMA) from different shard-rich horizons (SRH) in the four studied cores. Mean and standard deviation (Stdv.) are listed below each SRH. The compositional data are plotted in the TAS diagram (Figure 6A). H₂O was obtained through difference (100-total oxides).

Core/ Depth	Grain No.	SiO ₂	TiO ₂	Al ₂ O ₃	Cr ₂ O ₃	FeO	MnO	MgO	CaO	Na ₂ O	K ₂ O	P ₂ O ₅	NiO	H ₂ O	Total
AAS-22/8	NIO-1-1	71.66	0.04	12.04	0.01	1.05	0.06	0.05	0.77	1.34	4.62	0.00	0.00	8.36	91.64
(135-140)	NIO-1-2	72.08	0.06	11.66	0.00	0.95	0.05	0.07	0.79	0.63	4.11	0.01	0.04	9.55	90.45
	NIO-1-4	76.28	0.06	9.67	0.01	0.91	0.07	0.05	0.77	0.90	4.17	0.01	0.00	7.11	92.89
	NIO-1-5	76.55	0.07	10.97	0.03	0.93	0.06	0.06	0.74	0.99	4.18	0.01	0.02	5.40	94.61
	NIO-1-6	75.76	0.06	12.24	0.01	1.04	0.05	0.06	0.73	1.50	4.32	0.01	0.01	4.22	95.78
	Stdv.	2.39	0.01	1.04	0.01	0.06	0.01	0.01	0.03	0.35	0.21	0.01	0.01		
	Mean	74.46	0.06	11.31	0.01	0.97	0.06	0.06	0.76	1.07	4.28	0.01	0.01	6.93	93.07
AAS-22/8	NIO-2-1	73.84	0.06	12.37	0.04	0.87	0.08	0.06	0.75	1.53	4.16	0.00	0.00	6.27	93.74
(190-195)	NIO-2-2	72.98	0.04	12.54	0.00	0.88	0.04	0.06	0.82	1.44	4.53	0.01	0.00	6.66	93.35
	NIO-2-3	73.68	0.05	12.11	0.02	0.92	0.05	0.04	0.72	1.44	4.40	0.01	0.01	6.57	93.44
	NIO-2-4	72.63	0.06	12.36	0.01	0.93	0.07	0.05	0.77	1.30	4.32	0.01	0.00	7.49	92.51
	NIO-2-5	75.56	0.05	11.94	0.02	0.87	0.06	0.03	0.68	1.36	4.16	0.00	0.00	5.28	94.73
	NIO-2-6	73.13	0.06	12.61	0.01	0.91	0.04	0.04	0.81	0.77	4.01	0.00	0.01	7.61	92.39
	Stdv.	1.04	0.01	0.25	0.01	0.03	0.01	0.01	0.05	0.28	0.19	0.00	0.01		
	Mean	73.64	0.05	12.32	0.02	0.90	0.06	0.05	0.76	1.31	4.26	0.00	0.00	6.64	93.36
AAS-22/8	NIO-3-1	73.54	0.06	11.27	0.03	0.87	0.08	0.04	0.71	1.06	4.39	0.01	0.00	7.95	92.05
(205-210)	NIO-3-2	74.21	0.06	11.31	0.00	0.68	0.03	0.03	0.71	1.08	4.12	0.00	0.03	7.75	92.26
	NIO-3-3	74.48	0.09	11.94	0.02	0.99	0.07	0.05	0.75	1.13	3.98	0.00	0.00	6.50	93.51
	NIO-3-4	73.74	0.03	12.86	0.02	0.81	0.05	0.06	0.79	1.54	4.42	0.02	0.00	5.67	94.33
	NIO-3-5	74.36	0.05	11.82	0.00	0.87	0.05	0.04	0.70	1.31	4.54	0.01	0.00	6.26	93.74
	NIO-3-6	70.86	0.04	13.64	0.01	0.82	0.08	0.05	0.72	1.36	4.23	0.02	0.03	8.14	91.86
	Stdv.	1.36	0.02	0.93	0.01	0.10	0.02	0.01	0.04	0.19	0.21	0.01	0.02		
	Mean	73.53	0.05	12.14	0.01	0.84	0.06	0.04	0.73	1.25	4.28	0.01	0.01	7.04	92.96
AAS-22/8	NIO-4-1	73.83	0.07	11.48	0.00	0.90	0.08	0.04	0.71	1.07	4.51	0.00	0.03	7.28	92.72
(430-435)	NIO-4-2	76.70	0.05	11.05	0.01	0.83	0.06	0.03	0.60	0.97	4.02	0.00	0.00	5.69	94.32
	NIO-4-3	70.00	0.05	12.45	0.00	1.09	0.06	0.05	0.81	1.14	4.34	0.00	0.00	10.03	89.97
	NIO-4-6	76.97	0.06	9.76	0.00	0.86	0.04	0.05	0.67	0.53	3.99	0.01	0.03	7.03	92.97
	Stdv.	3.25	0.01	1.11	0.00	0.12	0.01	0.01	0.09	0.28	0.25	0.00	0.01		
	Mean	74.38	0.06	11.19	0.00	0.92	0.06	0.04	0.70	0.92	4.21	0.00	0.01	7.41	92.50
AAS-22/8	NIO-5-1	73.84	0.05	12.07	0.00	0.95	0.06	0.04	0.74	1.49	3.98	0.00	0.00	6.78	93.22
(485-490)	NIO-5-2	73.44	0.06	12.06	0.00	0.98	0.06	0.03	0.68	1.52	4.34	0.04	0.01	6.79	93.22
	NIO-5-3	73.68	0.06	12.30	0.00	0.96	0.03	0.06	0.71	1.29	3.97	0.00	0.01	6.93	93.07
	NIO-5-4	72.36	0.05	12.39	0.01	0.88	0.04	0.04	0.74	1.63	4.54	0.00	0.02	7.31	92.69
	NIO-5-5	73.27	0.07	12.12	0.01	0.96	0.05	0.04	0.76	1.27	4.27	0.00	0.01	7.18	92.82
	NIO-5-6	73.78	0.06	12.41	0.01	1.03	0.06	0.05	0.77	1.46	4.14	0.03	0.00	6.20	93.80
	Stdv.	0.55	0.01	0.16	0.00	0.05	0.01	0.01	0.03	0.14	0.22	0.02	0.01		
	Mean	73.39	0.06	12.22	0.00	0.96	0.05	0.04	0.74	1.45	4.20	0.01	0.01	6.86	93.14
AAS-22/8	NIO-7-1	74.97	0.05	11.58	0.00	0.80	0.06	0.05	0.71	1.29	3.89	0.00	0.00	6.62	93.38
(520-525)	NIO-7-2	73.63	0.07	12.38	0.00	0.93	0.03	0.06	0.75	1.48	4.35	0.00	0.02	6.31	93.69
	NIO-7-3	74.98	0.04	12.01	0.00	0.87	0.08	0.03	0.69	1.27	4.00	0.02	0.03	5.99	94.01
	NIO-7-4	73.95	0.05	12.41	0.03	0.97	0.06	0.04	0.75	1.47	4.18	0.00	0.03	6.08	93.93
	NIO-7-5	74.66	0.04	12.21	0.00	0.83	0.06	0.05	0.71	1.43	4.32	0.00	0.00	5.69	94.31
	NIO-7-6	74.10	0.05	12.23	0.00	0.90	0.05	0.05	0.70	1.43	4.06	0.00	0.00	6.44	93.56
	Stdv.	0.57	0.01	0.31	0.01	0.06	0.02	0.01	0.03	0.09	0.18	0.01	0.01		
	Mean	74.38	0.05	12.14	0.01	0.88	0.06	0.05	0.72	1.39	4.13	0.00	0.01	6.19	93.81
AAS-22/7	NIO-13-2	78.28	0.04	10.83	0.04	0.89	0.04	0.04	0.74	1.33	4.20	0.01	0.01	3.54	96.46
(0-5)	NIO-13-3	77.00	0.05	10.10	0.02	0.88	0.08	0.04	0.71	0.76	4.08	0.01	0.00	6.29	93.72
	NIO-13-6	74.54	0.05	11.84	0.00	1.03	0.04	0.07	0.84	1.13	4.13	0.00	0.00	6.34	93.66
	NIO-13-7	74.99	0.05	13.06	0.01	0.90	0.08	0.06	0.72	1.64	4.23	0.00	0.01	4.25	95.75

	NIO-13-8	74.46	0.07	12.39	0.00	0.88	0.08	0.04	0.72	1.59	4.32	0.00	0.04	5.42	94.59
	Stdv.	1.71	0.01	1.19	0.02	0.06	0.02	0.01	0.05	0.36	0.09	0.00	0.01		
	Mean	75.85	0.05	11.64	0.01	0.91	0.06	0.05	0.74	1.29	4.19	0.00	0.01	5.16	94.84
AAS-22/7	NIO-6-1	73.22	0.05	12.11	0.00	0.77	0.07	0.04	0.72	1.51	4.33	0.00	0.03	7.14	92.86
(220-225)	NIO-6-2	72.07	0.07	12.75	0.00	0.99	0.12	0.06	0.79	1.28	4.33	0.02	0.04	7.48	92.52
	NIO-6-3	72.06	0.05	11.98	0.02	0.98	0.03	0.04	0.72	1.35	4.31	0.04	0.01	8.43	91.57
	NIO-6-4	77.34	0.04	12.28	0.01	0.89	0.04	0.04	0.68	1.22	4.13	0.00	0.05	3.27	96.73
	NIO-6-5	75.70	0.05	11.87	0.01	0.98	0.02	0.04	0.77	1.41	4.34	0.02	0.00	4.79	95.21
	NIO-6-6	75.04	0.06	12.23	0.00	0.94	0.05	0.04	0.80	1.27	4.29	0.00	0.00	5.28	94.72
	Stdv.	2.14	0.01	0.31	0.01	0.08	0.04	0.01	0.05	0.11	0.08	0.02	0.02		
	Mean	74.24	0.05	12.20	0.01	0.92	0.06	0.04	0.75	1.34	4.29	0.01	0.02	6.06	93.94
AAS-22/5	NIO-14-1	75.13	0.04	13.15	0.00	0.99	0.07	0.07	0.79	1.61	4.31	0.01	0.00	3.83	96.18
(10-15)	NIO-14-2	73.29	0.02	12.07	0.01	0.88	0.10	0.04	0.67	1.33	4.29	0.01	0.01	7.29	92.71
	NIO-14-3	72.14	0.05	12.32	0.01	0.91	0.06	0.07	0.73	1.30	4.38	0.01	0.02	8.01	91.99
	NIO-14-4	72.56	0.08	12.43	0.02	0.85	0.07	0.06	0.76	1.29	4.25	0.00	0.00	7.63	92.37
	NIO-14-5	74.52	0.07	11.15	0.00	1.02	0.06	0.04	0.73	1.11	4.60	0.02	0.00	6.69	93.31
	NIO-14-6	75.72	0.05	11.73	0.00	0.88	0.06	0.05	0.66	1.37	4.23	0.02	0.01	5.23	94.77
	Stdv.	1.45	0.02	0.68	0.01	0.07	0.02	0.01	0.05	0.16	0.14	0.01	0.01		
	Mean	73.89	0.05	12.14	0.01	0.92	0.07	0.05	0.72	1.34	4.34	0.01	0.01	6.45	93.56
AAS-22/5	NIO-15-1	72.61	0.04	13.04	0.01	0.86	0.06	0.05	0.70	1.55	4.54	0.00	0.02	6.52	93.48
(110-115)	NIO-15-2	71.42	0.05	11.23	0.03	0.90	0.07	0.04	0.75	0.85	4.48	0.00	0.00	10.18	89.82
	NIO-15-3	75.65	0.05	12.09	0.00	0.83	0.05	0.05	0.72	1.16	4.01	0.00	0.02	5.37	94.63
	NIO-15-4	72.38	0.04	11.92	0.03	0.91	0.02	0.05	0.73	1.30	4.16	0.03	0.02	8.40	91.60
	NIO-15-5	74.06	0.06	12.17	0.00	1.00	0.06	0.05	0.71	1.34	4.11	0.00	0.02	6.43	93.57
	NIO-15-6	75.05	0.05	12.15	0.03	0.90	0.04	0.03	0.68	1.32	4.25	0.02	0.01	5.48	94.52
	Stdv.	1.66	0.01	0.58	0.01	0.06	0.02	0.01	0.02	0.23	0.21	0.01			
	Mean	73.53	0.05	12.10	0.02	0.90	0.05	0.04	0.72	1.25	4.26	0.01	0.01	7.06	92.94
AAS-22/5	NIO-16-1	72.16	0.18	12.41	0.01	1.65	0.13	0.31	1.77	1.13	1.16	0.02	0.00	9.09	90.91
(245-250)	NIO-16-2	72.50	0.04	11.79	0.05	0.81	0.09	0.05	0.70	1.44	4.24	0.00	0.00	8.31	91.69
	NIO-16-3	75.56	0.06	11.78	0.05	0.88	0.09	0.03	0.69	1.00	3.96	0.00	0.01	5.88	94.12
	NIO-16-4	73.44	0.11	12.03	0.01	0.86	0.05	0.10	0.69	1.02	4.22	0.02	0.00	7.45	92.55
	NIO-16-6	74.53	0.26	11.83	0.05	1.26	0.04	0.22	1.18	1.00	2.28	0.00	0.00	7.36	92.64
	Stdv.	1.417	0.090	0.266	0.024	0.358	0.036	0.118	0.476	0.186	1.387	0.011	0.003		
	Mean	73.64	0.13	11.97	0.03	1.09	0.08	0.14	1.01	1.12	3.17	0.01	0.00	7.62	92.38
AAS-22/3	NIO-8-1	74.94	0.05	12.03	0.00	0.84	0.10	0.05	0.68	1.44	4.42	0.02	0.00	5.43	94.57
(10-15)	NIO-8-2	76.96	0.05	10.84	0.00	0.86	0.06	0.05	0.74	0.98	4.47	0.00	0.00	4.98	95.02
	NIO-8-3	73.26	0.05	12.36	0.04	0.92	0.05	0.05	0.75	1.53	4.41	0.02	0.00	6.58	93.43
	NIO-8-4	72.49	0.06	12.88	0.00	0.91	0.05	0.07	0.87	1.61	4.48	0.02	0.00	6.57	93.43
	NIO-8-5	72.28	0.05	12.67	0.00	0.86	0.08	0.05	0.70	1.86	4.66	0.01	0.00	6.78	93.22
	NIO-8-6	72.53	0.06	11.99	0.00	0.92	0.05	0.05	0.85	1.39	4.34	0.00	0.02	7.81	92.20
	Stdv.	1.86	0.01	0.72	0.01	0.03	0.02	0.01	0.08	0.29	0.11	0.01	0.01		
	Mean	73.74	0.05	12.13	0.01	0.89	0.06	0.05	0.76	1.47	4.46	0.01	0.00	6.36	93.64
AAS-22/3	NIO-9-1	72.85	0.08	11.80	0.00	0.91	0.06	0.04	0.77	1.36	4.26	0.00	0.00	7.87	92.13
(60-65)	NIO-9-2	72.36	0.03	11.57	0.00	0.96	0.05	0.04	0.78	1.07	4.21	0.00	0.02	8.92	91.09
	NIO-9-3	72.88	0.06	12.11	0.00	1.07	0.07	0.05	0.75	1.31	3.97	0.00	0.01	7.73	92.27
	NIO-9-4	71.74	0.05	12.16	0.00	0.94	0.07	0.05	0.70	1.54	4.37	0.00	0.02	8.37	91.63
	NIO-9-5	72.02	0.03	12.06	0.00	0.87	0.07	0.04	0.74	1.38	4.09	0.00	0.00	8.69	91.31
	NIO-9-6	72.70	0.05	11.47	0.02	0.99	0.05	0.05	0.74	1.01	4.10	0.00	0.00	8.83	91.17
	Stdv.	0.47	0.02	0.29	0.01	0.07	0.01	0.00	0.03	0.20	0.14	0.00	0.01		
	Mean	72.42	0.05	11.86	0.00	0.96	0.06	0.05	0.75	1.28	4.17	0.00	0.01	8.40	91.60
AAS-22/3	NIO-10-1	74.05	0.04	12.40	0.01	0.89	0.07	0.05	0.80	1.41	4.35	0.01	0.00	5.92	94.08
(170-175)	NIO-10-2	72.53	0.06	12.25	0.00	0.75	0.06	0.07	0.82	1.36	4.08	0.03	0.00	8.00	92.00
	NIO-10-3	73.58	0.06	11.01	0.00	0.96	0.08	0.06	0.78	1.00	4.36	0.01	0.01	8.11	91.89
	NIO-10-4	75.08	0.06	11.06	0.00	0.83	0.04	0.04	0.74	1.15	4.31	0.02	0.02	6.64	93.36
	NIO-10-5	75.58	0.05	10.68	0.00	0.84	0.10	0.05	0.74	0.99	4.31	0.01	0.03	6.62	93.38
	NIO-10-6	72.95	0.07	11.51	0.01	0.83	0.04	0.06	0.77	1.09	4.22	0.00	0.00	8.46	91.54
	Stdv.	1.19	0.01	0.70	0.00	0.07	0.02	0.01	0.03	0.18	0.10	0.01	0.01		
	Mean	73.96	0.06	11.48	0.00	0.85	0.07	0.05	0.77	1.16	4.27	0.01	0.01	7.29	92.71

AAS-22/3	NIO-17-2	73.80	0.04	11.77	0.04	0.82	0.08	0.03	0.67	1.30	4.44	0.01	0.00	7.00	93.00
(285-290)	NIO-17-3	78.11	0.06	11.91	0.02	0.80	0.08	0.04	0.59	1.48	4.09	0.00	0.00	2.83	97.17
	NIO-17-6	73.64	0.07	11.82	0.00	0.84	0.04	0.06	0.77	1.34	4.53	0.00	0.00	6.88	93.12
	Stdv.	2.54	0.02	0.07	0.02	0.02	0.02	0.02	0.09	0.09	0.23	0.00	0.00		
	Mean	75.18	0.06	11.83	0.02	0.82	0.07	0.04	0.68	1.37	4.35	0.00	0.00	5.57	94.43
AAS-22/3	NIO-11-1	73.71	0.08	12.33	0.00	0.81	0.03	0.07	0.81	1.54	4.32	0.01	0.00	6.30	93.70
(295-300)	NIO-11-2	74.07	0.05	12.31	0.02	0.86	0.02	0.05	0.80	1.34	4.09	0.02	0.00	6.37	93.63
	NIO-11-3	74.60	0.06	11.88	0.00	0.77	0.05	0.05	0.67	1.42	4.31	0.02	0.00	6.18	93.82
	NIO-11-5	74.16	0.07	12.04	0.05	0.98	0.06	0.05	0.74	1.41	4.40	0.00	0.00	6.05	93.95
	NIO-11-6	74.57	0.05	11.76	0.00	0.95	0.10	0.05	0.69	1.36	4.26	0.00	0.00	6.23	93.77
	Stdv.	0.37	0.01	0.25	0.02	0.09	0.03	0.01	0.06	0.08	0.11	0.01	0.00		
	Mean	74.22	0.06	12.06	0.01	0.87	0.05	0.05	0.74	1.41	4.27	0.01	0.00	6.23	93.77
AAS-22/3	NIO-12-2	76.50	0.05	12.08	0.02	0.89	0.07	0.06	0.79	1.48	4.39	0.00	0.01	3.69	96.32
(325-330)	NIO-12-3	75.10	0.06	12.24	0.00	0.91	0.09	0.03	0.72	1.57	4.58	0.01	0.01	4.70	95.30
	NIO-12-4	74.98	0.06	11.54	0.01	1.09	0.07	0.04	0.70	1.16	4.53	0.00	0.00	5.83	94.17
	NIO-12-6	73.47	0.06	11.45	0.00	0.98	0.07	0.03	0.69	1.03	4.47	0.01	0.00	7.73	92.27
	Stdv.	1.24	0.00	0.39	0.01	0.09	0.01	0.01	0.04	0.26	0.08	0.00	0.00		
	Mean	75.01	0.06	11.83	0.01	0.97	0.07	0.04	0.72	1.31	4.49	0.00	0.00	5.49	94.51
AAS-22/3	NIO-18-1	74.33	0.06	12.18	0.01	0.97	0.02	0.05	0.74	1.38	4.44	0.00	0.00	5.81	94.19
(335-340)	NIO-18-2	73.49	0.04	12.65	0.00	0.97	0.07	0.04	0.68	1.53	4.39	0.00	0.02	6.11	93.89
	NIO-18-3	73.16	0.05	11.86	0.00	0.99	0.09	0.03	0.71	1.18	4.46	0.03	0.00	7.44	92.56
	NIO-18-5	73.79	0.05	11.90	0.00	1.01	0.06	0.05	0.69	1.36	4.43	0.04	0.00	6.62	93.38
	NIO-18-6	73.00	0.06	10.82	0.00	0.89	0.05	0.04	0.68	0.94	4.56	0.02	0.00	8.94	91.06
	Stdv.	0.53	0.01	0.67	0.00	0.05	0.03	0.01	0.03	0.22	0.06	0.02	0.01		
	Mean	73.55	0.05	11.88	0.00	0.97	0.06	0.04	0.70	1.28	4.46	0.02	0.00	6.98	93.02
AAS-22/3	NIO-19-1	74.80	0.07	12.40	0.00	0.96	0.06	0.05	0.78	1.50	4.67	0.00	0.00	4.71	95.29
(350-355)	NIO-19-2	74.04	0.03	11.82	0.00	0.99	0.03	0.04	0.75	1.33	4.38	0.03	0.03	6.54	93.46
	NIO-19-4	77.86	0.06	12.20	0.00	0.86	0.08	0.05	0.70	1.38	4.35	0.01	0.00	2.44	97.56
	NIO-19-5	75.36	0.06	11.72	0.00	1.04	0.04	0.05	0.71	1.18	4.45	0.00	0.03	5.37	94.63
	Stdv.	1.66	0.02	0.32	0.00	0.08	0.02	0.00	0.04	0.13	0.15	0.01	0.02		
	Mean	75.51	0.06	12.04	0.00	0.96	0.05	0.05	0.73	1.35	4.46	0.01	0.01	4.77	95.23
AAS-22/3	NIO-20-3	77.04	0.05	11.24	0.00	0.99	0.07	0.04	0.69	1.09	4.33	0.01	0.00	4.45	95.55
(365-370)	NIO-20-4	72.81	0.08	12.04	0.00	0.97	0.04	0.07	0.80	1.06	4.30	0.02	0.00	7.82	92.18
	NIO-20-5	75.21	0.05	12.36	0.00	0.96	0.06	0.08	0.80	1.56	4.51	0.02	0.02	4.38	95.62
	NIO-20-6	73.50	0.04	12.06	0.03	0.93	0.07	0.03	0.75	1.35	4.67	0.01	0.00	6.58	93.42
	Stdv.	1.89	0.02	0.48	0.02	0.03	0.01	0.02	0.05	0.24	0.17	0.01	0.01		
	Mean	74.64	0.05	11.92	0.01	0.96	0.06	0.06	0.76	1.26	4.45	0.01	0.00	5.81	94.19

Table 4: Correlation of the identified layers with paleomagnetic (Diehl et al 1987) and $\delta^{18}\text{O}$ dates from Dehn et al. (1991). YTT = Youngest Toba Tuff (74 ka), OTT = Oldest Toba Tuff (0.84 Ma).

Layer	Reported Ages	Calculated ages are based on the known layers YTT AND OTT (Pattan et al 2010) and the co-occurring microtektite layer of 0.77Ma (Prasad et al 2007).							
		AAS-22/8		AAS-22/7		AAS-22/5		AAS-22/3	
		Depth (cm)	Calculated Age (Ma)	Depth (cm)	Calculated Age (Ma)	Depth (cm)	Calculated Age (Ma)	Depth (cm)	Calculated Age (Ma)
A	0.071-0.110			0-5	0.074	10-15	0.074 ± 0.014	10-15	0.074 ± 0.014
B	0.071-0.121								
C	0.512-0.538	135-140	0.511 ± 0.008						
D	0.731-0.750	190-195	0.715 ± 0.008						
d	0.756-0.750								
E	0.774-0.780	205-210	0.77 ± 0.008	220-225	0.77 ± 0.008	110-115	0.77 ± 0.035	60-65	0.77 ± 0.035
F	1.273-1.294								
G	1.596-1.653	430-435	1.607 ± 0.008			245-250	1.64 ± 0.035		
		485-490	1.812 ± 0.008						
		520-525	1.942 ± 0.008						
H	2.238-2.265							170-175	2.23 ± 0.035
h	3.664-3.666							285-290	3.83 ± 0.035
I	4.124-4.131							295-300	3.97 ± 0.035
J	4.552-4.560							325-330	4.32 ± 0.035
K	4.666-4.667							335-340	4.48 ± 0.035
L	4.759-4.765							350-355	4.74 ± 0.035
M	5.062-5.063							365-370	4.95 ± 0.035

Reported Ages are as per Dehn et al (1991). Sedimentation rates for core AAS-22/8 is 2.69 mm/ka, for AAS-22/7 it is 0.34 mm/ka up to YTT and 3.1mm/ka from YTT to OTT. In the southern core AAS-22/5, it is 1.68mm/ka up to YTT and 1.43mm/ka from YTT to OTT. While the southernmost core AAS-22/3 has 1.68 mm/ka up to YTT and 0.718 mm/ka from YTT to OTT as reported (Pattan et al 2010).

Table 5: Geochemical composition of the glass shards reported as per the different layers encountered in the CIOB sediment.

Core	Depth/Layer	N	SiO ₂	TiO ₂	Al ₂ O ₃	Cr ₂ O ₃	FeO	MnO	MgO	CaO	Na ₂ O	K ₂ O	P ₂ O ₅	NiO	H ₂ O	Total
	A (YTT)	92	76.81	0.07	12.77	nd	nd	0.06	0.05	0.79	3.41	5.08	0.16	nd	nd	100.12
AAS-22/7	(0-5)	5	75.85	0.05	11.64	0.01	0.91	0.06	0.05	0.74	1.29	4.19	0.00	0.01	5.16	94.84
AAS-22/5	(10-15)	6	73.89	0.05	12.14	0.01	0.92	0.07	0.05	0.72	1.34	4.34	0.01	0.01	6.45	93.56
AAS-22/3	(10-15)	6	76.33	0.06	12.21	0.01	0.91	0.06	0.05	0.77	2.35	4.64	0.08	0.01	2.52	97.48
	B	NI														
	C (MTT)	18	77.57	0.06	12.24	nd	1.02	0.04	0.63	3.55	4.73	0.12	nd	nd		100
AAS-22/8	(135-140)	5	74.46	0.06	11.31	0.01	0.97	0.06	0.06	0.76	1.07	4.28	0.01	0.01	6.93	93.07
	D	13	74	0.07	11.76	nd	0.83	0	0.02	0.14	2.79	2.79	0.01	nd	4.92	95.1
AAS-22/8	(190-195)	6	73.64	0.05	12.32	0.02	0.90	0.06	0.05	0.76	1.31	4.26	0.00	0.00	6.64	93.36
	d	NI														
	E (OTT)	19	77.33	0.05	12.7	nd	nd	0.07	0.07	0.77	2.84	5.18	0.2	nd	nd	99.37
AAS-22/8	(205-210)	6	73.53	0.05	12.14	0.01	0.84	0.06	0.04	0.73	1.25	4.28	0.01	0.01	7.04	92.96
AAS-22/7	(220-225)	6	74.24	0.05	12.20	0.01	0.92	0.06	0.04	0.75	1.34	4.29	0.01	0.02	6.06	93.94
AAS-22/5	(110-115)	6	73.53	0.05	12.10	0.02	0.90	0.05	0.04	0.72	1.25	4.26	0.01	0.01	7.06	92.94
AAS-22/3	(60-65)	6	73.74	0.05	12.13	0.01	0.89	0.06	0.05	0.76	1.47	4.46	0.01	0.00	6.36	93.64
	F	NI														
	G	9	73.31	0.13	11.38	nd	0.69	nd	0.04	0.59	3.07	4.91	0.02	nd	5.86	94.14
AAS-22/8	(430-435)	4	74.38	0.06	11.19	0.00	0.92	0.06	0.04	0.70	0.92	4.21	0.00	0.01	7.41	92.50
AAS-22/5	(245-250)	5	73.64	0.13	11.97	0.03	1.09	0.08	0.14	1.01	1.12	3.17	0.01	0.00	7.62	92.38
	H	13	72.76	0.04	11.64	nd	0.75	nd	0.02	0.45	3.35	4.3	0.02	nd	6.66	93.34
AAS-22/3	(170-175)	6	72.42	0.05	11.86	0.00	0.96	0.06	0.05	0.75	1.28	4.17	0.00	0.01	8.40	91.60
	h	8	73.07	0.05	11.65	nd	0.66	nd	0.01	0.64	3.22	4.72	0.02	nd	5.91	94.1
AAS-22/3	(285-290)	3	73.96	0.06	11.48	0.00	0.85	0.07	0.05	0.77	1.16	4.27	0.01	0.01	7.29	92.71
	I	5	73.63	0.04	11.89	nd	0.62	nd	0.03	0.67	3.11	4.35	0	nd	5.66	94.34
AAS-22/3	(295-300)	5	75.18	0.06	11.83	0.02	0.82	0.07	0.04	0.68	1.37	4.35	0.00	0.00	5.57	94.43
	J	10	73.02	0.08	11.92	nd	0.69	nd	0.08	0.82	3.16	4.4	0.03	nd	5.81	94.2
AAS-22/3	(325-330)	4	75.01	0.06	11.83	0.01	0.97	0.07	0.04	0.72	1.31	4.49	0.00	0.00	5.49	94.51
	K	10	71.87	0.08	11.62	nd	1.02	nd	0.04	0.61	3.43	4.35	0.02	nd	6.98	93.02
AAS-22/3	(335-340)	5	73.55	0.05	11.88	0.00	0.97	0.06	0.04	0.70	1.28	4.46	0.02	0.00	6.98	93.02
	L	8	68.06	0.35	12.7	nd	2.38	nd	0.26	1.4	3.77	4.42	0.06	nd	6.63	93.38
AAS-22/3	(350-355)	4	75.51	0.06	12.04	0.00	0.96	0.05	0.05	0.73	1.35	4.46	0.01	0.01	4.77	95.23
	M	10	71.33	0.11	11.85	nd	0.97	nd	0.11	1.05	3.31	4.05	0.04	nd	7.19	92.81
AAS-22/3	(365-370)	4	74.64	0.05	11.92	0.01	0.96	0.06	0.06	0.76	1.26	4.45	0.01	0.00	5.81	94.19

The list of referenced data: Pattan et al (1992) (YTT); Westgate et al (1988) (Middle Toba Tuff, MTT); Pattan et al (2010) (OTT); while Layer D, and Layers G to M are from Dehn et al (1991). The layers represented by NI = are Not Identified in the study area hence no data are provided. nd= data not defined. n = Number of shards analysed. The average values are obtained from our data (Table 3). See text for explanation.

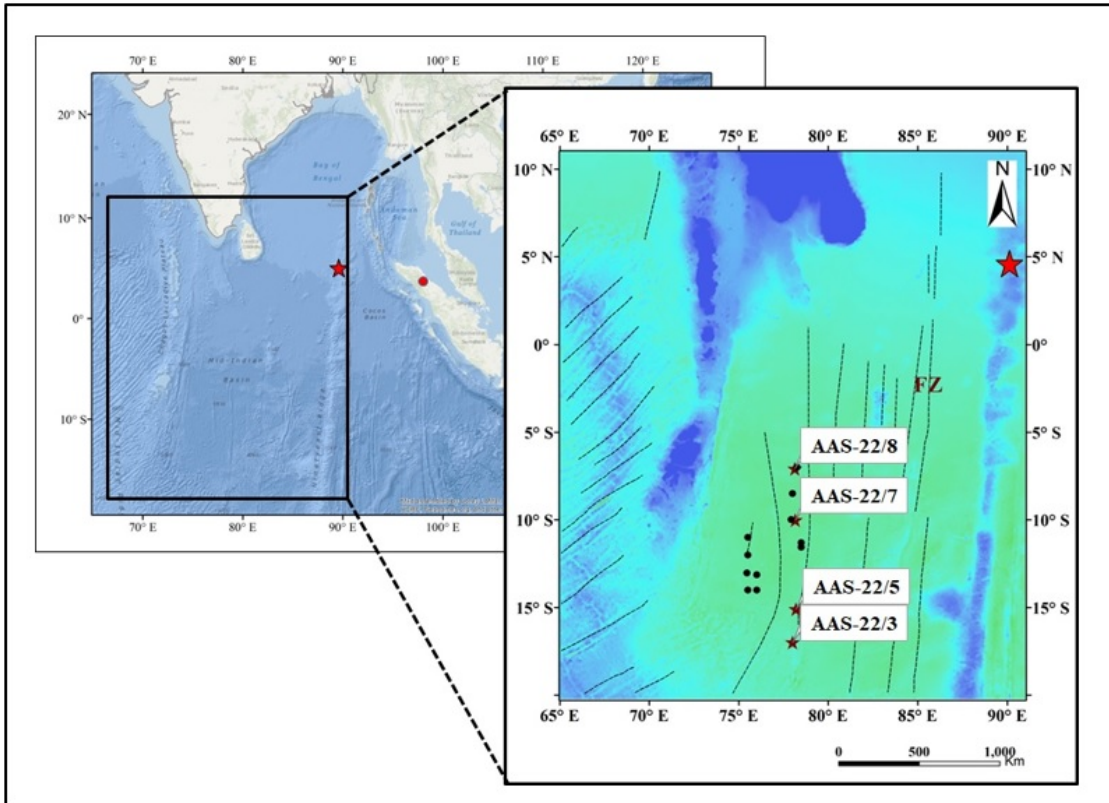


Figure 1

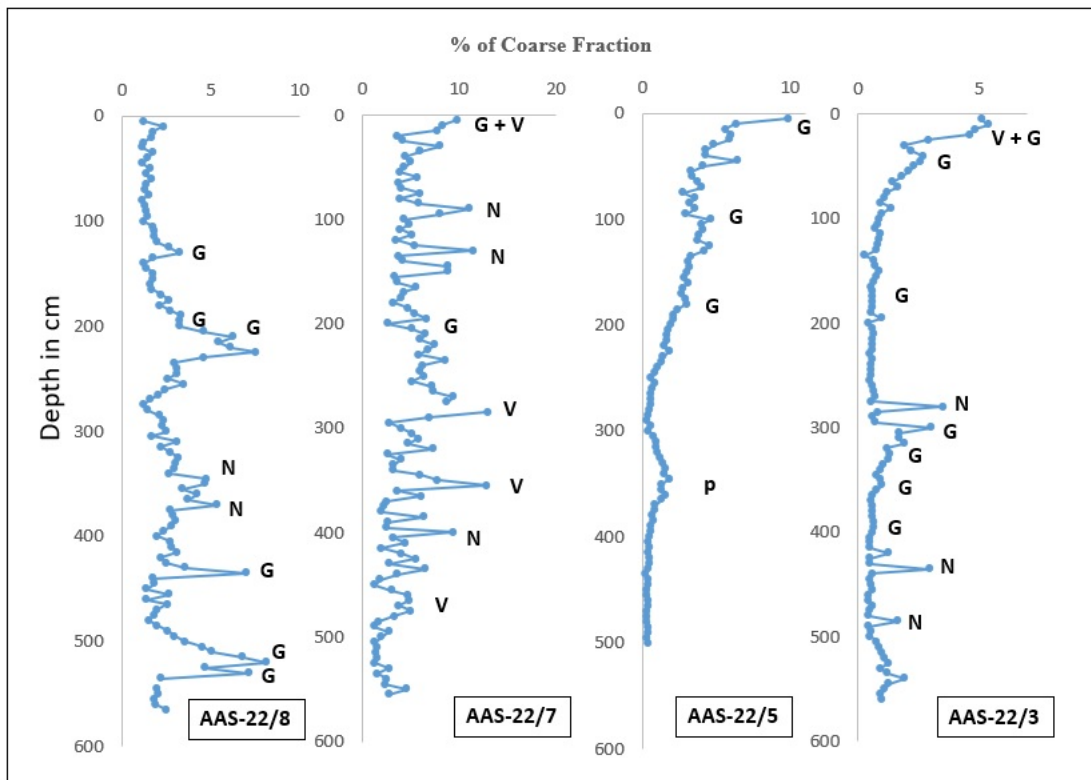


Figure 2

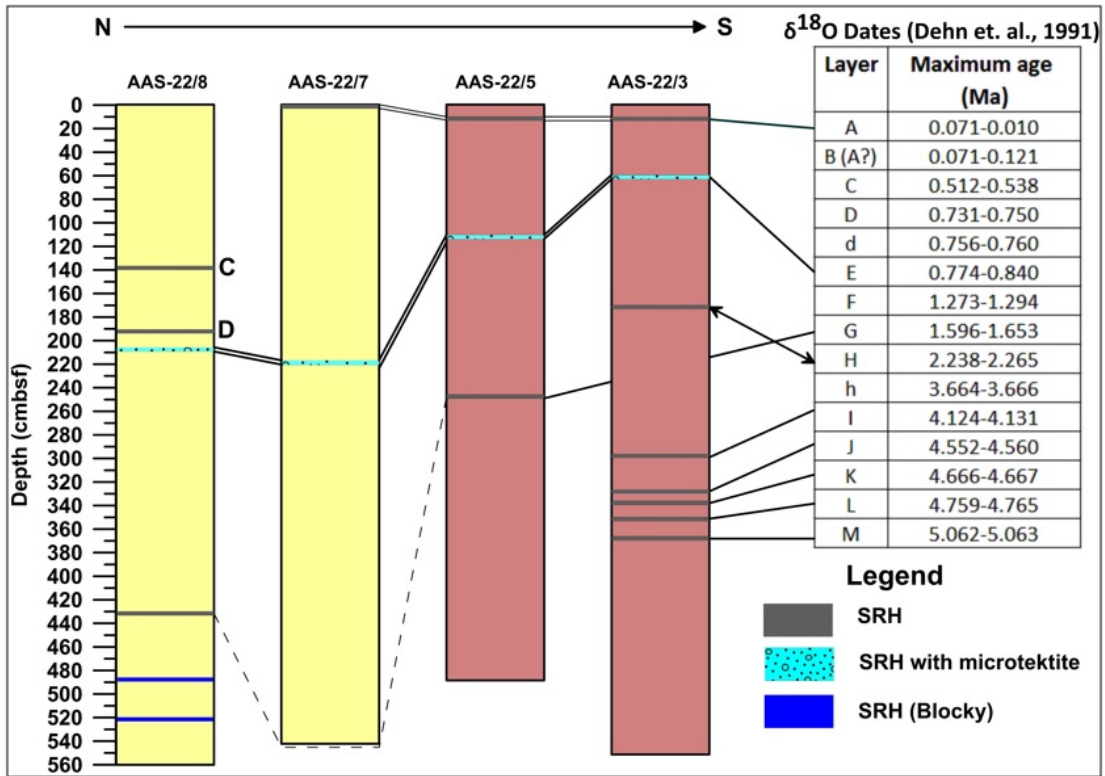


Figure 3

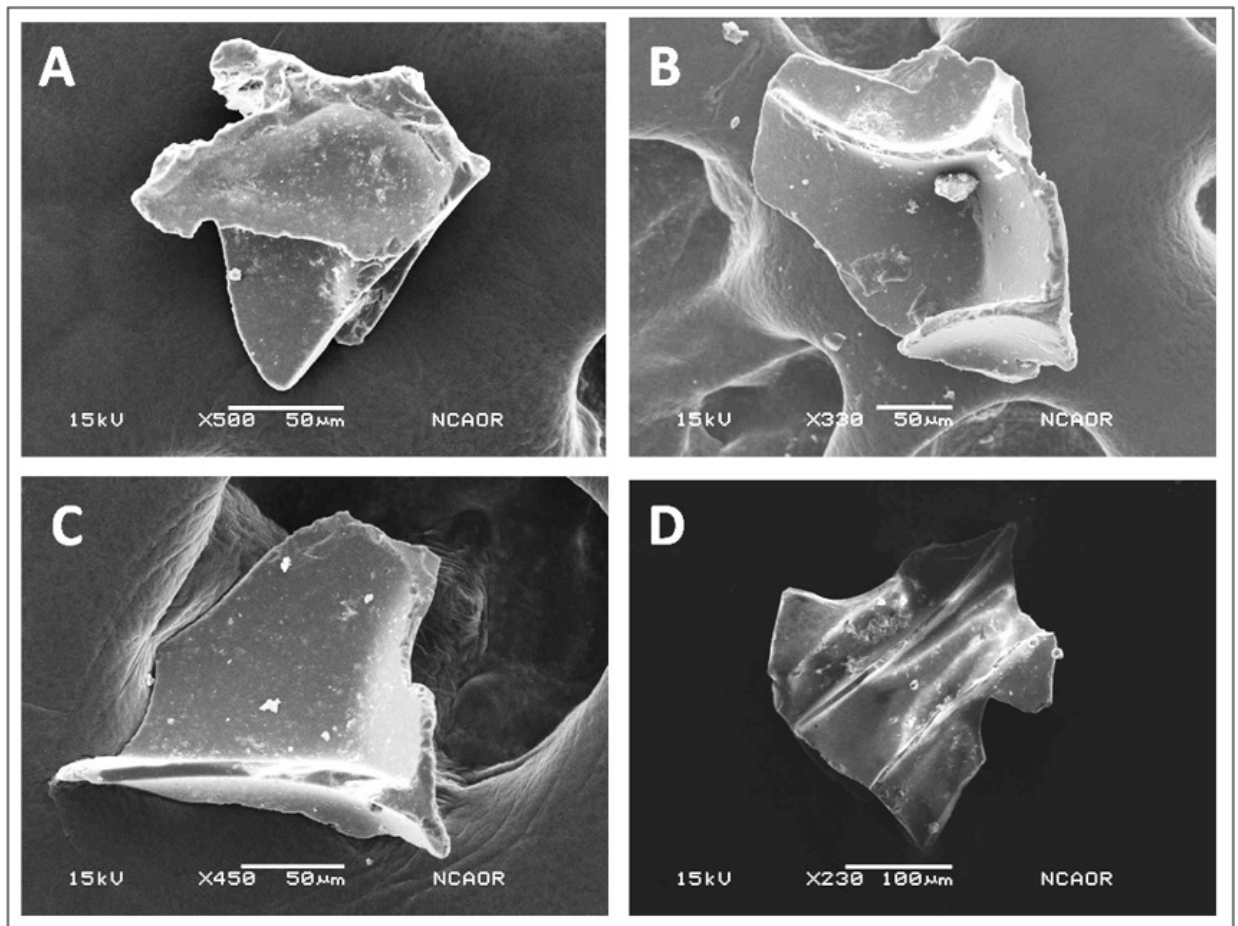


Figure 4

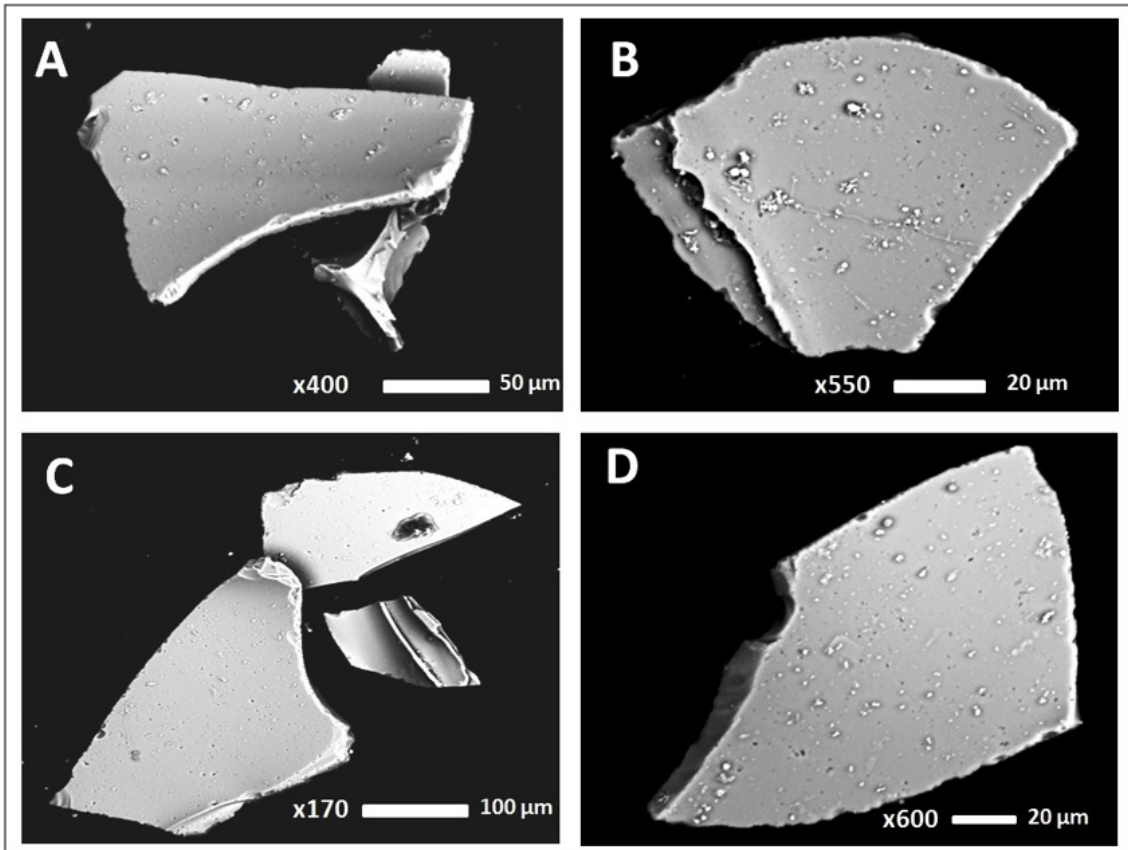


Figure 5

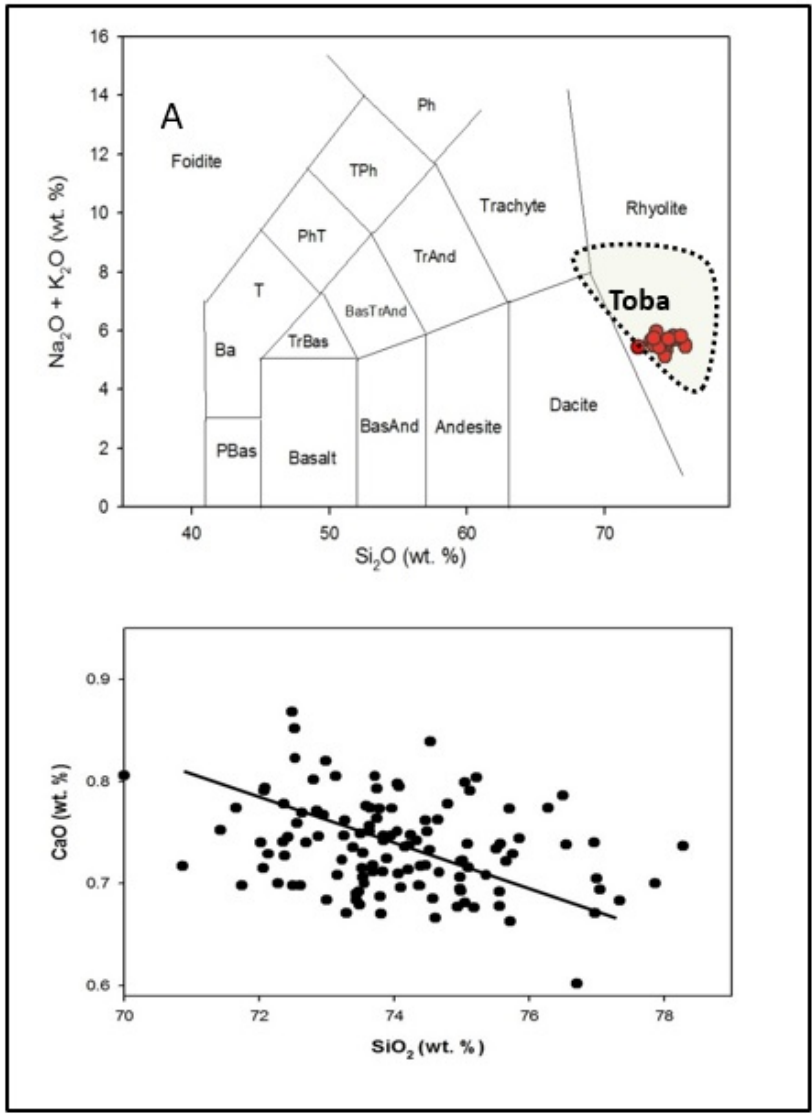


Figure 6

Captions for Figures

Figure 1 (Left panel) Map showing the major physiographic features of the CIOB. The referred site ODP 758 has been marked in red solid star symbol. The Toba caldera is marked with red solid dot. (Right panel) The detailed map of the study area with locations of sediment cores marked as solid deep red star while the referenced sites are marked with black solid dot (details are provided in Table 1).

Figure 2. Down-core variation of $>63 \mu\text{m}$ fraction percentage in the four studied cores of the CIOB. Legends: N=Micronodules, G=Glass shards, V=Volcanic material, P=Palagonite Grains

Figure 3. Cores AAS-22/8 and AAS-22/7 are sited in the siliceous domain and are marked by the pale yellow body while cores AAS-22/5 and AAS-22/3 are from the transition of red clay and red clay marked deep-red. SRH (Shard-Rich Horizons) identified in the studied cores are depicted here. The Layer E (OTT) along with microtektites is used as a datum plane to calculate the sedimentation rate (marked with light blue colour). Linear extrapolations of the rate of sedimentation have helped in comparing the identified layers with ODP Site 758 (Dehn et al 1991) tephrochronology. The two SRH (blue) occurring in the core AAS-22/8 with type II shards could be of an intra basinal origin while the other SRH are derived from Toba eruptions.

Figure 4. SEM images of volcanic shards from the study area.

Type I: The shards are dominantly cusped, (A) bubble wall and shows Y shape intersections (B-D).

Figure 5. SEM images of volcanic shards from the study area occurring at depth 458-490 and 520-525 cm in the core AAS-22/8

Type II: The shards show a platy and blocky morphology (A-D).

Figure 6. Geochemical classification diagram of glass shards from all the four cores used in the present study. The Toba field line is drawn using the data provided in Table 6.

A) TAS diagram show the analysed shards from the four cores to be rhyolitic. The nomenclature fields are after Le Bas et al. (1986). Abbreviations: Ph = Phonolite; TPh = Tephriphonolite; PhT = Phonotephrite, T = Tephrite; Ba = Basanite; PBas = microbasalt; TrBas = Trachybasalt; BaTrAnd = Basaltic trachyandesite; TrAnd = Trachyandesite; BasAnd = Basaltic andesite.

B) Plot of SiO_2 against CaO.